Journal of Computational Physics 228 (2009) 4510–4531

Contents lists available at ScienceDirect

Journal of Computational Physics

journal homepage: www.elsevier.com/locate/jcp

Verified predictions of shape sensitivities in wall-bounded turbulent flows by an adaptive finite-element method

A. Hay *, D. Pelletier, R. Di Caro

Département de Génie Mécanique, Ecole Polytechnique de Montréal, Montréal, Québec, Canada H3C3A7

ARTICLE INFO

Article history:
Received 15 April 2008
Received in revised form 24 December 2008
Accepted 14 March 2009
Available online 27 March 2009

Keywords:
Sensitivity Analysis
Sensitivity Equation Method
Turbulent flows
RANS equations
k-epsilon model
Wall functions
Adaptive finite-element method
Verification and Validation

ABSTRACT

A Continuous Sensitivity Equation (CSE) method is presented for shape parameters in turbulent wall-bounded flows modeled with the standard k–ϵ turbulence model with wall functions. Differentiation of boundary conditions and their complex dependencies on shape parameters, including the two-velocity scale wall functions, is presented in details along with the appropriate methodology required for the CSE method. To ensure accuracy, grid convergence and to reduce computational time, an adaptive finite-element method driven by asymptotically exact error estimations is used. The adaptive process is controlled by error estimates on both flow and sensitivity solutions. Firstly, the proposed approach is applied on a problem with a closed-form solution, derived using the Method of the Manufactured Solution to perform Code Verification. Results from adaptive grid refinement studies show Verification of flow and sensitivity solvers, error estimators and the adaptive strategy. Secondly, we consider turbulent flows around a square cross-section cylinder in proximity of a solid wall. We examine the quality of the numerical solutions by performing Solution Verification and Validation. Then, Sensitivity Analysis of these turbulent flows is performed to investigate the ability of the method to deal with non-trivial geometrical changes. Sensitivity information is used to estimate uncertainties in the flow solution caused by uncertainties in the shape parameter and to perform fast evaluation of flows on nearby configurations.

1. Introduction

Sensitivity Analysis (SA) has been the topic of active research for many years because of its numerous industrial applications. In design optimization, it refers to the gradient of the cost functions with respect to design variables which can be efficiently obtained through adjoint methods. In a more general framework, sensitivities are the derivatives of the dependent variables with respect to any (physical or numerical) parameter. They are more general in the sense that the derivatives of cost functions can be deduced from the sensitivities of dependent variables; the reciprocal being false. We refer to them as *flow sensitivities*. The body of work on SA has shown that it provides improved insights into the physic of complex problems and allows for a better understanding of them.

Irrespective of the approach employed, computing sensitivities is more involved for parameters that influence the problem through the modification of its geometry. They are referred to as *shape parameters* as opposed to *value parameters*. Indeed, a number of difficulties arises when considering shape parameters both from the theoretical and the practical side that will be discussed in what follows.

* Corresponding author. Address: ICAM, Virginia Tech, Blacksburg 24060-0531, Virginia, USA. Tel.: +1 540 231 5054.
E-mail addresses: hay@vt.edu (A. Hay), dominique.pelletier@polymtl.ca (D. Pelletier), richard.di-caro@polymtl.ca (R. Di Caro).

0021-9991/$ - see front matter © 2009 Elsevier Inc. All rights reserved.
doi:10.1016/j.jcp.2009.03.022

There are several approaches for computing sensitivities: (1) Finite Differences (FD); (2) Complex Variable Method (CVM); and (3) Sensitivity Equation Methods (SEM). The first option requires only evaluations of dependent variables and computes their derivatives by finite differences. This simple approach requires minimal additional development. However, it is costly because the problem at hand must be solved at least as many times as there are parameters. Furthermore, numerical evaluations of sensitivities of pointwise quantities is often difficult because of technical problems arising from non-matching meshes. However, the main disadvantage of this approach is that the calculation of derivatives may suffer from subtractive cancellation errors leading to large errors in the evaluations if the parameter perturbations are too small. This approach is often used as a verification tool for the other methodologies (see e.g. [1–3]).

The CVM is similar to the FD idea with the exception that a complex perturbation is taken. The key improvement is that computed derivatives are not affected by round-off errors [4]. However, the CVM does not offer a saving of resources when compared to using FD [5] since the problem must be solved at a perturbed state for each parameter. Furthermore, the required memory for the solver essentially doubles due to the use of complex declarations of floating point variables (the CPU time of the original solver is also increased by a significant factor).

The last option is provided by the SEM which corresponds to numerically solving a set of equations for the sensitivities. These equations are obtained by differentiation of the (discrete or continuous) equations for the dependent variables. Since they are always linear, the SEM always compute a sensitivity for a fraction of the cost of computing the flow making these methodologies very attractive. In the Continuous Sensitivity Equation (CSE) approach, the governing equations are first differentiated and then discretized, whereas in the Discrete Sensitivity Equation (DSE) approach, discretization is performed prior to differentiation. The advantages of each methodology and their differences have been extensively discussed in the literature (see e.g. [6,7]). One of the main advantages of the DSE approach is that it can be handled through Automatic Differentiation (AD). It is a powerful approach because the code for calculating sensitivities is almost automatically generated from the code for computing dependent variables. Yet, in many cases, implementation requires user interventions to ensure efficiency of the resulting sensitivity code both in terms of accuracy and CPU time. See [8–10] for more details on AD and on the most common softwares. One of the main advantage of the CSE method is that it avoids the differentiation of non-differentiable terms arising from discretization schemes such as limiters, blending functions or stabilization terms (since differentiation is performed on the continuous flow equations). Furthermore, the continuous approach offers more flexibility at the discretization stage. Here, we present a CSE approach.

When a shape parameter a is considered, independent variables (say $\mathbf{x}$) depend on a. Dependent variables (say $\mathbf{u}$) always depend both on $\mathbf{x}$ and a : $\mathbf{u}(\mathbf{x}, a)$. Hence, for a shape parameter, one can consider either the *Eulerian* sensitivity $\partial\mathbf{u}/\partial a$ (partial derivative of $\mathbf{u}$ with respect to a) or the *Lagrangian* sensitivity $D\mathbf{u}/Da$ (total derivative of $\mathbf{u}$ with respect to a). The major difficulty in using Lagrangian sensitivities is the requirement to define and manage the domain deformation induced by the boundary displacement when the parameter changes (the definition being non-unique). Eulerian sensitivities avoid this delicate issue but special attention must be paid when deriving and evaluating boundary conditions. It is worth noting that the DSE methods presented in the literature all use Lagrangian sensitivities which lead to the need for evaluating mesh sensitivities. This requires the delicate issue of differentiating the mesh generation code or mesh deformation procedure which is both involved and computationally demanding. To circumvent these difficulties, we propose the use of the Eulerian sensitivities and present a suitable methodology for handling boundary conditions for the corresponding Sensitivity Equations in turbulent flow problems. Moreover, this approach simplifies the use of adaptive grid methods which have proved to be extremely powerful for achieving mesh independent solutions of complex problems [11,12].

In Computational Fluid Mechanics (CFD), there is a wealth of publication on SEM for laminar flows (see e.g. Refs. [13,6,14–18,3]). However, the situation is quite different for the case of turbulent flows for which there is a paucity of literature. The additional equations for turbulence modeling greatly increase the level of complexity of the system of PDE and its discretization. The DSE approach has been applied to turbulent flows and value parameters using AD in Refs. [19,20] and to shape parameters using hand-differentiation in Refs. [21,22]. The CSE method for turbulent flows and value parameters is presented in Refs. [23–25]. To the authors' knowledge, this work is the first attempt to derive a CSE method for turbulent flows and shape parameters.

To this end, wall-bounded turbulent flows are modeled with the RANS equations and the standard k–ϵ turbulence model with wall functions using two velocity scales. The CSE are obtained by direct differentiation of this set of PDE and their associated boundary conditions. There are two major challenges when treating shape parameters. The first difficulty arises from the differentiation of wall functions which is not straightforward due to their complex shape parameter dependencies. For example, the boundary condition for the flow in the tangential direction is prescribed as a function of the tangential velocity (mixed or Robin boundary condition). Secondly, it leads to a difficult requirement: the accurate evaluation of the first and second-order derivatives of the velocity at the boundary. Duvigneau and Pelletier [26] have recently proposed a constrained Taylor-series least-squares procedure to achieve accurate boundary gradients for laminar flows. For this work, we extend the constrained Taylor-series least-squares procedure to wall-bounded turbulent flows (see Section 5.4).

The accurate evaluation of flow and shape sensitivity solutions of wall bounded turbulent problems is a tedious task. Indeed, the flow exhibits features whose strength and location are difficult to capture. They are also hard to predict *a priori* so that a good mesh is difficult to design *ab initio*. This difficulty is compounded when sensitivity variables are added because their features are less intuitive than that of the flow variables. Furthermore, the transpiration terms in their boundary conditions result in very thin regions where sensitivity variables exhibit sharp variations. And, when considering several design parameters, each sensitivity has its own region of rapid variations. Hence, their successful computation requires appropriate

numerics. Here, we combine numerical techniques and state-of-the-art computational practices to yield and demonstrate a powerful approach to compute flow and shape sensitivity in turbulent regime.

On the numerical side we use higher-order stabilized finite-element discretization with an adaptive remeshing procedure to provide grid resolution for all flow and sensitivity variables. This is achieved by using asymptotically exact error estimates for all flow and sensitivity unknowns to drive the adaption process. Hence, computational meshes have grid size distributions adapted to capture all rapid variations in flow and sensitivity variables.

To demonstrate the reliability of the numerical techniques as well as the accuracy of their predictions, the methodology is used within a rigorous framework for Verification and Validation. Roache [27] gives an excellent overview of the subject which is comprised of three essential steps: (1) Code Verification, (2) Solution Verification, (3) Validation. There are all performed here for the wall-bounded turbulent flow and sensitivity problem at hand. The Method of Manufactured Solution (MMS) is used for Code Verification of the flow and sensitivity solvers, the error estimators for the flow and sensitivities and the adaptive remeshing modules in a single grid refinement study. To our knowledge, this is the first reported Verification by the MMS of sensitivity solver for wall-bounded turbulent flows. Mesh adaptation also automates much of the Verification process thus relieving the analyst of the tedious tasks of generating the complex meshes required by the grid refinement study. Results indicate that highly refined meshes are required to ensure grid independence of the finite-element predictions. In the case of shape parameters in turbulent flows up to 600,000 grid points, adaptively located, are needed to achieve mesh independence.

The paper is organized as follows. First, the flow equations are presented in Section 2 and their associated boundary conditions in Section 3. Section 4 presents the Continuous Sensitivity Equations. In Section 5, we detail the shape sensitivity boundary conditions and the proper methodology required for parameter dependent boundaries. Section 6 introduces the stabilized finite-element formulation, the error estimation technique and the adaptive remeshing procedure. The proposed approach is first verified in Section 7 (Code Verification) on a problem with a closed-form solution derived using the Method of the Manufactured Solution [28,29]. As will be shown, the closed-form solution allows for the simultaneous Verification of the flow and sensitivity solver, the adaptive procedure and the error estimators and any post-processing. In Section 8, the method is applied to turbulent flows around a square obstacle in proximity of a solid wall. We first perform Solution Verification and Validation to assess the accuracy of the numerical predictions. Then, sensitivities are used to predict changes in the flow response arising from non-trivial geometrical changes. In particular, we use sensitivity information to (1) estimate uncertainties in the flow solution caused by uncertainties in the shape parameters and (2) to perform fast evaluation of flows on nearby configurations.

2. Governing equations

The flows of interest are described by the steady Reynolds-Averaged Navier–Stokes (RANS) equations on a domain Ω. The momentum and mass conservation laws are written as:

$$\rho\mathbf{u}\cdot\nabla\mathbf{u} = -\nabla p + \nabla\cdot\tau(\mathbf{u}) + \mathbf{f} \tag{1}$$

$$\nabla\cdot\mathbf{u} = 0 \tag{2}$$

where ρ is the density, $\mathbf{u}$ the velocity, p the pressure and $\mathbf{f}$ the volumetric forces. The viscous stress tensor is defined according to Newton's law and the Reynolds stress from the first order turbulence model approximation. Denoting by μ the molecular dynamic viscosity and μ_t the dynamic eddy-viscosity, the resulting shear stress tensor τ in Eq. (1) is:

$$\tau(\mathbf{u}) = (\mu+\mu_t)[\nabla\mathbf{u} + (\nabla\mathbf{u})^T]$$

The system is closed by evaluating the turbulent viscosity using the k–ϵ model by:

$$\mu_t = \rho C_\mu \frac{k^2}{\epsilon} \tag{3}$$

To preserve positivity of the dependent variables, we work with the logarithmic form of these equations [30]. This can be viewed as using the following change of dependent variables:

$$\mathcal{K} = \ln(k) \quad \text{and} \quad \mathcal{E} = \ln(\epsilon) \tag{4}$$

The transport equations for the logarithmic variables are:

$$\rho\mathbf{u}\cdot\nabla\mathcal{K} = \nabla\cdot\left[\left(\mu+\frac{\mu_t}{\sigma_k}\right)\nabla\mathcal{K}\right] + \left(\mu+\frac{\mu_t}{\sigma_k}\right)\nabla\mathcal{K}\cdot\nabla\mathcal{K}\mu_t e^{-\mathcal{K}}P - \rho^2 C_\mu\frac{e^{\mathcal{K}}}{\mu_t} + q_{\mathcal{K}} \tag{5}$$

$$\rho\mathbf{u}\cdot\nabla\mathcal{E} = \nabla\cdot\left[\left(\mu+\frac{\mu_t}{\sigma_\epsilon}\right)\nabla\mathcal{E}\right] + \left(\mu+\frac{\mu_t}{\sigma_\epsilon}\right)\nabla\mathcal{E}\cdot\nabla\mathcal{E} + \rho C_1 C_\mu e^{\mathcal{K}-\mathcal{E}}P - C_2\rho e^{\mathcal{E}-\mathcal{K}} + q_{\mathcal{E}} \tag{6}$$

In which the production of turbulence P is defined as:

$$P = \nabla\mathbf{u} : [\nabla\mathbf{u} + (\nabla\mathbf{u})^T]$$

Table 1
Constant of the turbulence model.

σ_k	σ_ϵ	$C_{\epsilon 1}$	$C_{\epsilon 2}$	C_μ
1.0	1.3	1.44	1.92	0.09

The constants appearing in these equations are set to the standard values proposed by Launder and Spalding [31] and are given in Table 1. Note that Eqs. (5) and (6) are equivalent to the original equations of the turbulence model; only the computational variables are different. Hence, the turbulence model remains unchanged. The eddy-viscosity expressed with the logarithmic variables is:

$$\mu_t = \rho C_\mu e^{2\mathcal{K}-\mathcal{E}} \tag{7}$$

Finally, the volumetric forces $\mathbf{f}$ in Eq. (1) and the source terms $q_\mathcal{K}$ and $q_\mathcal{E}$ in Eqs. (5) and (6) are used for Code Verification purposes in the framework of the Method of the Manufactured Solution in Section 7. For real flow problems, as the one considered in Section 8, they are set to zero.

3. Flow boundary conditions

This section focuses on the boundary conditions associated with the governing equations that apply on the boundary Γ of the domain Ω. While fairly standard, we provide details on the boundary conditions because they will prove necessary in developing the boundary conditions for the sensitivity problem.

3.1. Classical Dirichlet and Neumann boundary conditions

Boundaries of Ω that are not walls are subjected to standard Dirichlet and Neumann boundary conditions that are imposed on boundaries Γ_D and Γ_N respectively. For instance:

- *Dirichlet boundary conditions:*

$$\mathbf{u} = \overline{\mathbf{u}}; \quad \mathcal{K} = \ln(\beta_k); \quad \mathcal{E} = \ln(\beta_\epsilon) \tag{8}$$

- *Neumann boundary conditions:*

$$[-pI + \tau(\mathbf{u})] \cdot \hat{\mathbf{n}} = \overline{\mathbf{t}}; \quad \left[\left(\mu + \frac{\mu_t}{\sigma_k}\right)\nabla\mathcal{K}\right] \cdot \hat{\mathbf{n}} = 0; \quad \left[\left(\mu + \frac{\mu_t}{\sigma_\epsilon}\right)\nabla\mathcal{E}\right] \cdot \hat{\mathbf{n}} = 0 \tag{9}$$

where $\hat{\mathbf{n}}$ is an outward unit normal vector at the boundary, I the second-order identity tensor, β_k and β_ϵ small constants and $\overline{\mathbf{t}}$ the imposed surface traction.

3.2. Wall boundary conditions

The standard k–ϵ turbulence model is not valid when the turbulent Reynolds number is low, as it is the case in near-wall regions. Wall functions are used to describe the solution in these areas. The computational boundary is set at a distance d from the physical wall boundary. The gap between these two boundaries is the region where the flow is represented by the wall functions instead of being solved. In the remainder, the computational wall boundary will be referred to as the wall and quantities evaluated at it will be identified with the subscript w. We use the two-velocity scale wall functions described by Chabard [32] and Ignat et al. [33] and presented in what follows.

A wall function expresses the value of u^+, the non-dimensional velocity parallel to the solid wall, as a function of y^+, the non-dimensional normal distance from the physical wall:

$$u^+ = \frac{1}{\kappa}\ln(Ey^+) \quad \text{for } y^+ > 10.8 \tag{10}$$

where κ is the Karman constant and E a roughness parameter (for smooth walls: $\kappa = 0.42$ and $E = 9.0$). The variables u^+ and y^+ are defined as follows:

$$y^+ = \frac{\rho d u_k}{\mu} \quad \text{and} \quad u^+ = \frac{u_t}{u_{**}} \tag{11}$$

where $u_t = \mathbf{u}\cdot\hat{\mathbf{t}}$ denotes the tangential velocity, d is the normal distance to the physical wall and $u_{**} = \sqrt{\tau_w/\rho}$ the friction velocity. The specific value of d where the wall function is applied is chosen so that y^+ lies within the range of validity of the wall function (i.e. $30 < y^+ < 300$) [34]. A velocity scale based on the turbulence kinetic energy is computed by (see Ref. [32] for details):

$$u_k = C_\mu^{\frac{1}{4}} k_w^{\frac{1}{2}} = C_\mu^{\frac{1}{4}} \exp\left(\frac{\mathcal{K}_w}{2}\right) \tag{12}$$

The boundary conditions associated to the governing equations are:

- flow boundary condition in the normal direction: The normal velocity is set to zero.

$$\mathbf{u}\cdot\hat{\mathbf{n}} = 0 \tag{13}$$

- flow boundary condition in the tangential direction: In the tangential direction the wall functions lead to a mixed boundary condition relating the tangential velocity to the wall shear stress. The two-velocity scale wall functions result in a linear relationship between the shear stress along the boundary τ_w and the tangential velocity u_t:

$$[(\tau\cdot\hat{\mathbf{n}})\cdot\hat{\mathbf{t}}]_{wall} = \tau_w = \rho u_k u_{**} = \frac{\rho u_k}{\frac{1}{\kappa}\ln\left(E\frac{\rho d u_k}{\mu}\right)} u_t \tag{14}$$

- boundary condition for $\mathcal{K}$: The $\mathcal{K}$-equation is solved with a zero auxiliary flux boundary condition. This condition arises from the fact that the wall shear stress is considered constant in the wall functions region (i.e. $0 < y^+ < 300$) [34]. This Neumann condition is required to compute the distribution of u_k along the wall.

$$\left(\mu + \frac{\mu_t}{\sigma_k}\right)\nabla\mathcal{K}\cdot\hat{\mathbf{n}} = 0 \tag{15}$$

- boundary condition for $\mathcal{E}$: The boundary condition for the logarithm of ϵ is the logarithm of the usual Dirichlet boundary condition for the turbulence kinetic energy dissipation rate at walls but the velocity scaled u_k is used instead of u_{**}.

$$\mathcal{E} = \ln\left(\frac{u_k^3}{\kappa d}\right) \tag{16}$$

4. Continuous Sensitivity Equations

The Continuous Sensitivity Equations (CSE) are derived formally by direct differentiation of the flow equations (Eqs. (1) and (2)) and the turbulence variables equations (Eqs. (5) and (6)) with respect to an arbitrary parameter a. Thus, we treat any variable $\mathbf{u}$ as a function of both space and parameter a. This dependency is denoted by $\mathbf{u} = \mathbf{u}(\mathbf{x}; a)$. The sensitivities are defined as the partial (Eulerian) derivatives:

$$\mathbf{s_u} = \frac{\partial\mathbf{u}}{\partial a};\quad s_p = \frac{\partial p}{\partial a};\quad s_\mathcal{K} = \frac{\partial\mathcal{K}}{\partial a};\quad s_\mathcal{E} = \frac{\partial\mathcal{E}}{\partial a} \tag{17}$$

Then, CSE governing these sensitivity fields are written as:

$$\rho'\mathbf{u}\cdot\nabla\mathbf{u} + \rho(\mathbf{s_u}\cdot\nabla\mathbf{u} + \mathbf{u}\cdot\nabla\mathbf{s_u}) = -\nabla s_p + \nabla\cdot\tau(\mathbf{s_u}) + \nabla\cdot\tau'(\mathbf{u}) + \mathbf{f}^s \tag{18}$$

$$\nabla\cdot\mathbf{s_u} = 0 \tag{19}$$

$$\begin{aligned}
&\rho'\mathbf{u}\cdot\nabla\mathcal{K} + \rho(\mathbf{s_u}\cdot\nabla\mathcal{K} + \mathbf{u}\cdot\nabla s_\mathcal{K}) \\
&\quad = \nabla\cdot\left[\left(\mu' + \frac{\mu_t'}{\sigma_k} - \frac{\mu_t\sigma_k'}{\sigma_k^2}\right)\nabla\mathcal{K} + \left(\mu + \frac{\mu_t}{\sigma_k}\right)\nabla s_\mathcal{K}\right] + \left(\mu' + \frac{\mu_t'}{\sigma_k} - \frac{\mu_t\sigma_k'}{\sigma_k^2}\right)\nabla\mathcal{K}\cdot\nabla\mathcal{K} \\
&\qquad + 2\left(\mu + \frac{\mu_t}{\sigma_k}\right)\nabla\mathcal{K}\cdot\nabla s_\mathcal{K} + e^{-\mathcal{K}}(\mu_t' P + \mu_t P' - \mu_t P s_\mathcal{K}) - \rho e^{\mathcal{E}-\mathcal{K}}\left(2\frac{\rho'}{\rho} + \frac{C_\mu'}{C_\mu} + s_\mathcal{K} - \frac{\mu_t'}{\mu_t}\right) + q_\mathcal{K}^s
\end{aligned} \tag{20}$$

$$\begin{aligned}
&\rho'\mathbf{u}\cdot\nabla\mathcal{E} + \rho(\mathbf{s_u}\cdot\nabla\mathcal{E} + \mathbf{u}\cdot\nabla s_\mathcal{E}) \\
&\quad = \nabla\cdot\left[\left(\mu' + \frac{\mu_t'}{\sigma_\epsilon} - \frac{\mu_t\sigma_\epsilon'}{\sigma_\epsilon^2}\right)\nabla\mathcal{E} + \left(\mu + \frac{\mu_t}{\sigma_\epsilon}\right)\nabla s_\mathcal{E}\right] + \left(\mu' + \frac{\mu_t'}{\sigma_\epsilon} - \frac{\mu_t\sigma_\epsilon'}{\sigma_\epsilon^2}\right)\nabla\mathcal{E}\cdot\nabla\mathcal{E} + 2\left(\mu + \frac{\mu_t}{\sigma_\epsilon}\right)\nabla\mathcal{E}\cdot\nabla s_\mathcal{E} \\
&\qquad + \rho C_{\epsilon1} C_\mu e^{\mathcal{K}-\mathcal{E}} P\left(\frac{\rho'}{\rho} + \frac{C_{\epsilon1}'}{C_{\epsilon1}} + \frac{C_\mu'}{C_\mu} + s_\mathcal{K} - s_\mathcal{E} + \frac{P'}{P}\right) - C_{\epsilon2}\rho e^{\mathcal{E}-\mathcal{K}}\left(\frac{C_{\epsilon2}'}{C_{\epsilon2}} + \frac{\rho'}{\rho} + s_\mathcal{E} - s_\mathcal{K}\right) + q_\mathcal{E}^s
\end{aligned} \tag{21}$$

the fluid property derivatives being denoted by a $(\prime)$ and account for all explicit and implicit dependencies; and:

$$\tau'(\mathbf{u}) = (\mu' + \mu_t')[\nabla\mathbf{u} + (\nabla\mathbf{u})^T]$$

$$\tau(\mathbf{s_u}) = (\mu + \mu_t)[\nabla\mathbf{s_u} + (\nabla\mathbf{s_u})^T]$$

$$P' = 2\nabla\mathbf{s_u} : [\nabla\mathbf{u} + (\nabla\mathbf{u})^T]$$

where the sensitivity of the eddy-viscosity is given by:

$$\mu_t' = \mu_t\left(\frac{\rho'}{\rho} + \frac{C_\mu'}{C_\mu} + 2s_\mathcal{K} - s_\mathcal{E}\right) \tag{22}$$

$\mathbf{f}^s, q^s_\mathcal{K}$ and $q^s_\mathcal{E}$ are the sensitivity of the volumetric forces and source terms in Eqs. (1), (5) and (6) respectively. Finally, the sensitivities of the turbulence variables and those of their logarithms are related through:

$$s_\mathcal{K} = \frac{s_k}{k}; \qquad s_\mathcal{E} = \frac{s_\epsilon}{\epsilon} \tag{23}$$

5. Shape sensitivity boundary conditions

To complete the description of the sensitivity problem, the boundary conditions presented in Section 3 are differentiated in the same way. However, if a is a shape parameter, the position of a boundary point is parameter dependent. As their name indicates, boundary conditions are only defined on the boundary of the domain and arise from physical considerations during the mathematical modeling of the problem. Furthermore, since the position of boundary points changes with a, the differentiation must therefore be performed while following the boundaries through their deformations. In other words, the total (or Lagrangian) derivative must be used. Thus, the differentiation should account for the fact that both the boundary location and the boundary condition depends on a.

Consequently, the parameter dependent boundaries must be properly parameterized. Some geometrical issues linked to shape parameters are first addressed in the next subsection before presenting the differentiation of the flow boundary conditions. For a complete mathematical analysis of problems related to the evolution of domains, the interested readers is referred to Refs. [35,36].

5.1. Describing parameter dependent boundaries

For a shape parameter, the position of points on the boundary Γ of the computational domain depends on the parameter of interest a. The boundary segment Γ is parameterized by ξ, the curvilinear coordinate of a point on Γ (the arc length is often used). With this definition, the parameter a controls the shape of Γ while ξ determines the location of a point on Γ. Therefore, any point $\hat{\mathbf{X}}$ of the boundary segment depends both on a and ξ:

$$\Gamma(a) = \{\hat{\mathbf{X}}(\xi, a) | \xi \in [\xi_0, \xi_1]\} \tag{24}$$

For a parameterization of this form, the unit normal and tangent vectors $\hat{\mathbf{n}}(\xi, a)$ and $\hat{\mathbf{t}}(\xi, a)$ are usually expressed in terms of the derivatives of $\hat{\mathbf{X}}$ with respect to ξ. Any change to a will affect all these geometrical quantities. If one follows a given point on Γ, ξ remains constant as a varies to change the shape of Γ as illustrated in Fig. 1. Thus, the total derivatives simplify to:

$$\frac{D\hat{\mathbf{X}}}{Da}(\xi, a) = \frac{\partial\hat{\mathbf{X}}}{\partial a}(\xi, a)$$
$$\frac{D\hat{\mathbf{n}}}{Da}(\xi, a) = \frac{\partial\hat{\mathbf{n}}}{\partial a}(\xi, a)$$
$$\frac{D\hat{\mathbf{t}}}{Da}(\xi, a) = \frac{\partial\hat{\mathbf{t}}}{\partial a}(\xi, a)$$

where D/Da denotes the total derivative with respect to a.

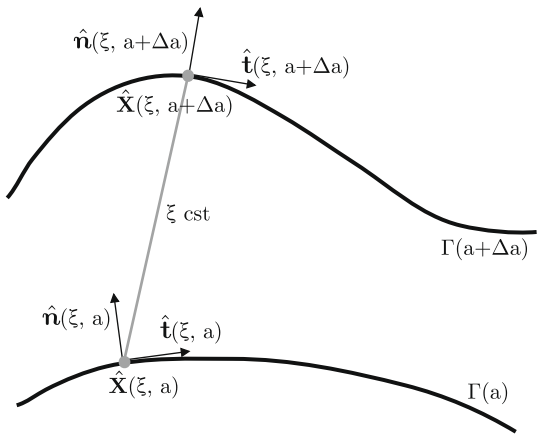

Fig. 1. Notations relative to boundary surface.

Now let ϕ be any solution variable or physical property and $\bar{\phi}$ its imposed value (in the case of a Dirichlet boundary condition: $\phi(\widehat{\mathbf{X}}, a) = \bar{\phi}(\widehat{\mathbf{X}}, a)$) on a parameter dependent boundary segment. The total derivative of this constraint is:

$$\frac{D\phi}{Da} = \frac{D\bar{\phi}}{Da}$$

where $D\bar{\phi}/Da$ is analytically known from the user-defined flow Dirichlet boundary condition. Using the chain rule, the total derivative of $\phi(\widehat{\mathbf{X}}(\xi, a), a)$ can be expressed as:

$$\frac{D\phi}{Da}(\widehat{\mathbf{X}}(\xi, a), a) = \frac{\partial\phi}{\partial a} + \nabla\phi \cdot \frac{\partial\widehat{\mathbf{X}}}{\partial a}$$

From this, the boundary condition for the (Eulerian) sensitivity of ϕ is obtained as the difference of $D\bar{\phi}/Da$ (which is analytically known) and a transpiration term accounting for the modification of the shape of the boundary:

$$\frac{\partial\phi}{\partial a} = \frac{D\bar{\phi}}{Da} - \nabla\phi \cdot \frac{\partial\widehat{\mathbf{X}}}{\partial a} \tag{25}$$

In general, the transpiration conditions involve the geometric sensitivities $\left(\frac{\partial\widehat{\mathbf{X}}}{\partial a}, \frac{\partial\hat{\mathbf{n}}}{\partial a}\right.$ and $\left.\frac{\partial\hat{\mathbf{t}}}{\partial a}\right)$ on the boundary curves. Note that, since we specify the parameterization of the boundary shape, these derivatives are well defined and easily computed.

5.2. Classical Dirichlet and Neumann boundary conditions

We first present the derivation of the classical Dirichlet and Neumann boundary conditions (Eqs. (8) and (9)). Sensitivity boundary conditions are obtained from relation (25) expressing the relationship between the total derivative and the sensitivity $\frac{\partial\phi}{\partial a}$. Doing so, the following boundary conditions are obtained.

- *Dirichlet boundary condition on Γ_D:*

$$\begin{aligned}
\mathbf{s}_{\mathbf{u}} &= \frac{D\bar{\mathbf{u}}}{Da} - \nabla\mathbf{u} \cdot \frac{\partial\widehat{\mathbf{X}}}{\partial a} \\
s_{\mathcal{K}} &= \frac{\beta_k'}{\beta_k} - \nabla\mathcal{K} \cdot \frac{\partial\widehat{\mathbf{X}}}{\partial a} \\
s_{\mathcal{E}} &= \frac{\beta_\epsilon'}{\beta_\epsilon} - \nabla\mathcal{E} \cdot \frac{\partial\widehat{\mathbf{X}}}{\partial a}
\end{aligned} \tag{26}$$

- *Neumann boundary condition on Γ_N:*

$$\begin{aligned}
&[-s_p\mathbf{I} + \tau'(\mathbf{u}) + \tau(\mathbf{s}_{\mathbf{u}})] \cdot \hat{\mathbf{n}} = \frac{D\bar{\mathbf{t}}}{Da} - [-p\mathbf{I} + \tau(\mathbf{u})] \cdot \frac{\partial\hat{\mathbf{n}}}{\partial a} - \left[\nabla[-p\mathbf{I} + \tau(\mathbf{u})] \cdot \frac{\partial\widehat{\mathbf{X}}}{\partial a}\right] \cdot \hat{\mathbf{n}} \\
&\left[\left(\mu' + \frac{\mu_t'}{\sigma_k} - \frac{\mu_t\sigma_k'}{\sigma_k^2}\right)\nabla\mathcal{K} + \left(\mu + \frac{\mu_t}{\sigma_k}\right)\nabla s_{\mathcal{K}}\right] \cdot \hat{\mathbf{n}} \\
&\quad = -\left[\nabla\mu \cdot \frac{\partial\widehat{\mathbf{X}}}{\partial a} + \frac{\nabla\mu_t \cdot \frac{\partial\widehat{\mathbf{X}}}{\partial a}}{\sigma_k}\right]\nabla\mathcal{K} \cdot \hat{\mathbf{n}} - \left(\mu + \frac{\mu_t}{\sigma_k}\right)\left[\nabla\mathcal{K} \cdot \frac{\partial\hat{\mathbf{n}}}{\partial a} + \nabla(\nabla\mathcal{K}) \cdot \frac{\partial\widehat{\mathbf{X}}}{\partial a} \cdot \hat{\mathbf{n}}\right] \\
&\left[\left(\mu' + \frac{\mu_t'}{\sigma_\epsilon} - \frac{\mu_t\sigma_\epsilon'}{\sigma_\epsilon^2}\right)\nabla\mathcal{E} + \left(\mu + \frac{\mu_t}{\sigma_\epsilon}\right)\nabla s_{\mathcal{E}}\right] \cdot \hat{\mathbf{n}} = -\left[\nabla\mu \cdot \frac{\partial\widehat{\mathbf{X}}}{\partial a} + \frac{\nabla\mu_t \cdot \frac{\partial\widehat{\mathbf{X}}}{\partial a}}{\sigma_\epsilon}\right]\nabla\mathcal{E} \cdot \hat{\mathbf{n}} - \left(\mu + \frac{\mu_t}{\sigma_\epsilon}\right)\left[\nabla\mathcal{E} \cdot \frac{\partial\hat{\mathbf{n}}}{\partial a} + \nabla(\nabla\mathcal{E}) \cdot \frac{\partial\widehat{\mathbf{X}}}{\partial a} \cdot \hat{\mathbf{n}}\right]
\end{aligned} \tag{27}$$

5.3. Wall function boundary conditions for sensitivities

The differentiation of the wall boundary conditions presented in Section 3 leads to the following boundary conditions for CSE.

- *flow sensitivity boundary condition in the tangential direction:*

$$\left[\left(\frac{\partial\tau}{\partial a} \cdot \hat{\mathbf{n}}\right) \cdot \hat{\mathbf{t}}\right]_w = \left(\rho' + \nabla\rho \cdot \frac{\partial\widehat{\mathbf{X}}}{\partial a}\right)u_k u_{**} + \rho u_k \frac{Du_{**}}{Da} + \rho u_{**}\frac{Du_k}{Da} - \tau \cdot \frac{\partial\hat{\mathbf{n}}}{\partial a} \cdot \hat{\mathbf{t}} - \tau \cdot \hat{\mathbf{n}} \cdot \frac{\partial\hat{\mathbf{t}}}{\partial a} - \left[\left(\nabla\tau \cdot \frac{\partial\widehat{\mathbf{X}}}{\partial a}\right) \cdot \hat{\mathbf{n}}\right] \cdot \hat{\mathbf{t}} \tag{28}$$

with the total derivatives of the velocity scales given by:

$$\frac{Du_k}{Da} = u_k\left[\frac{C'_\mu}{4C_\mu} + \frac{1}{2k_w}\left(s_k + \nabla k \cdot \frac{\partial \widehat{\mathbf{X}}}{\partial a}\right)\right] = u_k\left[\frac{C'_\mu}{4C_\mu} + \frac{1}{2}\left(s_\mathcal{K} + \nabla \mathcal{K} \cdot \frac{\partial \widehat{\mathbf{X}}}{\partial a}\right)\right] \tag{29}$$

$$\frac{Du_{**}}{Da} = \frac{\kappa}{\ln\left(\frac{E\rho d u_k}{\mu}\right)}\left\{\frac{\kappa' u_t}{\kappa} + \left(\mathbf{s_u} + \nabla \mathbf{u} \cdot \frac{\partial \widehat{\mathbf{X}}}{\partial a}\right)\cdot \hat{\mathbf{t}} + \mathbf{u}\cdot\frac{\partial \hat{\mathbf{t}}}{\partial a} - \frac{u_t}{\ln\left(\frac{E\rho d u_k}{\mu}\right)}\left[\frac{E'}{E} + \frac{d'}{d} + \frac{1}{u_k}\frac{Du_k}{Da} + \frac{\left(\rho' + \nabla\rho\cdot\frac{\partial \widehat{\mathbf{X}}}{\partial a}\right)}{\rho} - \frac{\left(\mu' + \nabla\mu\cdot\frac{\partial \widehat{\mathbf{X}}}{\partial a}\right)}{\mu}\right]\right\} \tag{30}$$

Note that (28) is a mixed boundary condition since $\left(\frac{\partial \tau}{\partial a}\cdot\hat{\mathbf{n}}\right)\cdot\hat{\mathbf{t}}$ is related to $\mathbf{s_u}\cdot\hat{\mathbf{t}}$ through $\frac{Du_{**}}{Da}$.

- *flow sensitivity boundary condition in the normal direction:*

$$\mathbf{s_u}\cdot\hat{\mathbf{n}} = -\left(\nabla\mathbf{u}\cdot\frac{\partial\widehat{\mathbf{X}}}{\partial a}\right)\cdot\hat{\mathbf{n}} - \mathbf{u}\cdot\frac{\partial\hat{\mathbf{n}}}{\partial a} \tag{31}$$

- boundary condition for $s_\mathcal{K}$:

$$\left[\left(\mu' + \frac{\mu'_t}{\sigma_k} - \frac{\mu_t\sigma'_k}{\sigma_k^2}\right)\nabla\mathcal{K} + \left(\mu + \frac{\mu_t}{\sigma_k}\right)\nabla s_\mathcal{K}\right]\cdot\hat{\mathbf{n}} = -\left[\nabla\mu\cdot\frac{\partial\widehat{\mathbf{X}}}{\partial a} + \frac{\nabla\mu_t\cdot\frac{\partial\widehat{\mathbf{X}}}{\partial a}}{\sigma_k}\right]\nabla\mathcal{K}\cdot\hat{\mathbf{n}} - \left(\mu + \frac{\mu_t}{\sigma_k}\right)\left[\nabla\mathcal{K}\cdot\frac{\partial\hat{\mathbf{n}}}{\partial a} + \nabla(\nabla\mathcal{K})\cdot\frac{\partial\widehat{\mathbf{X}}}{\partial a}\cdot\hat{\mathbf{n}}\right] \tag{32}$$

- boundary condition for $s_\mathcal{E}$:

$$s_\mathcal{E} = \frac{3}{u_k}\frac{Du_k}{Da} - \frac{\kappa'}{\kappa} - \frac{d'}{d} - \nabla\mathcal{E}\cdot\frac{\partial\widehat{\mathbf{X}}}{\partial a} \tag{33}$$

5.4. Computing boundary flow gradients for the sensitivity boundary conditions

As can be seen, for shape parameters, first derivatives of the flow and turbulence variables are needed to evaluate Dirichlet boundary conditions and second derivatives are required for evaluating Neumann or Robin boundary conditions. Unfortunately, this introduces numerical difficulties since only approximate boundary gradients are available from the flow solver. Accurate spatial gradients can be obtained in the interior of the computational domain with an *a posteriori* gradient projection technique (which is already used for error estimation). However, this technique does not yield accurate derivatives on boundaries.

A methodology to produce accurate boundary flow gradients was recently proposed by Duvigneau and Pelletier [26]. It consists in a least-squares reconstruction, using Taylor-series as basis functions, that is constrained to satisfy the flow boundary conditions through the method of Lagrange multipliers. It has been shown that one must use at least 3^{rd} order Taylor-series defined over patches of four layers of neighboring elements to achieve sufficient accuracy for the Dirichlet sensitivity boundary conditions and Taylor-series expansion of degree 6 on a 8-layer patch when Neumann conditions are imposed (see Ref. [26] for details). For this work, we have extended the constrained Taylor-series least-squares procedure to wall-bounded turbulent flows. This essentially involves two steps. First, the reconstruction procedure is also applied to the turbulence variables in the standard k–ϵ turbulence model. Second, the Taylor-series least-squares procedure is modified to enforce constraints ensuring that the reconstructed solution fields satisfy the wall function boundary conditions as required to yield consistent boundary flow gradients. Thus, the higher-order reconstructed solution variables satisfy the boundary conditions.

In Sections 7 and 8, boundary conditions for the sensitivity problems are computed using a 6th order Taylor-series least-squares reconstruction of flow variables on 8-layered patches. It will be shown that it ensures a sufficiently accurate evaluation of transpiration terms in the sensitivity boundary conditions.

6. Finite-element formulation and adaptive remeshing

The RANS equations and the logarithmic form of the turbulence equations are solved by a finite-element method. The velocity and the logarithmic turbulence variables are discretized using 6-nodded quadratic elements. Fluid pressure is discretized by piecewise linear continuous functions (Taylor-Hood element). For high Reynolds number, the equations are dominated by convection and the standard Galerkin discretization may lead to non-physical oscillations and convergence difficulties. Hence, some form of upwinding is required. This is done by using the Streamline Upwind/Petrov–Galerkin

(SUPG) stabilized formulation initially proposed by Brooks and Hughes [37] and further improved by Ilinca et al. [38]. The discretization of the flow equations leads to a system of non-linear algebraic equations which are linearized by Newton's method. All linear algebraic systems are solved using a sparse direct solver.

Because the Sensitivity Equations correspond to the linearization of the flow equations (alike the Jacobian in the Newton–Raphson method for the non-linear RANS equations), they are comprised of similar terms (convection, diffusion, etc). Hence, the same numerical techniques can be used to solve both the original and sensitivity problems so that no additional numerical technique is necessary. Furthermore, it eases the extension of an existing flow code to solve also the sensitivity equations. There is no particular difficulty in solving the sensitivity equations. In terms of computational cost, the sensitivity solutions are computed for a fraction of the cost of the flow since only one linear system needs to be solved. Moreover, the sensitivity problem is not subjected to convergence issues as it may be the case for the set of RANS equations. It should also be noted that for shape parameters, the sensitivity problems for two different parameters only differ from their boundary conditions. As a consequence, the matrix of the linear systems is the same for all parameters and the difference between linear systems is restricted to their right-hand sides. Thus, when using a direct solver, the LU decomposition has only to be performed once for the first parameter. Computing the sensitivity for any additional parameter only requires to build the system right-hand side and to perform the backward substitution. Hence, their is almost no CPU time overhead in computing shape sensitivities for several parameters. This makes our Eulerian approach to shape sensitivity very attractive compared to the more classical Lagrangian approaches (for which they are additional source terms in the equations that depends on the parameter so that matrices for two different parameters are not the same).

The accuracy of the finite-element approximation is directly related to the local mesh size (see Refs. [39,11]). An adaptive remeshing procedure is employed to improve the accuracy by refining the mesh in regions of high error in the flow and sensitivity variables. Regions targeted for refinement are identified by the so-called Zhu–Zienkiewicz (ZZ) error estimator [40,41] which evaluates estimates in elemental error norms. The ZZ error estimator belongs to the family of post-processing techniques (or least-squares-based recovery techniques) [27,42]. Although simple, recovery-based estimators perform surprisingly well in practice if a proper norm of the error is used [43,42,44].

Error estimates are obtained by a local least-squares reconstruction of the solution derivatives for the velocity and pressure fields and the logarithms of turbulence variables. Note that, an error estimate for the eddy-viscosity is also constructed since slowly varying fields of $\mathcal{K}$ and $\mathcal{E}$ may result in rapid variation of μ_t.

Once error estimates are obtained for all dependent variables (flow and sensitivities), an optimal mesh size distribution is determined for each variable using the asymptotic convergence rate of the finite-element method and the principle of equidistribution of the error so that each element has the same contribution to the norm of the total error [11]. The minimum element size predicted for all flow and sensitivity variables is selected to generate a new mesh by an advancing front method. This is performed in an iterative fashion, beginning with a coarse mesh and producing a sequence of meshes which reduce the error by a constant factor over that of the previous mesh. Note that refining on both the flow and its sensitivities is of crucial importance in the present context. Indeed, the flow variables and their sensitivities do not generally exhibit the same locations of rapid variations (and each sensitivity with respect to a given parameter has its own region of rapid variations). Consequently, the region of high errors on a given mesh are generally not the same for each flow variable and each sensitivity variable. Thus, to compute accurate solutions for all variables, we calculate and drive the adaptive process with as many error estimators as there are dependent variables involved in the problem at hand. The minimum element size predicted by all the dependent variables is selected on a given element. The computational domain is then re-meshed using an advancing front technique. Details of this adaptive remeshing procedure may be found in the literature [39,11,24,44].

7. Verification by the Method of the Manufactured Solution

We first assess the proposed numerical methodology and its implementation in this section. To that end, we used the Method of the Manufactured Solution (MMS) as proposed by Roache [27,28] to perform *Code Verification*. As will be shown, the closed-form solution enables the simultaneous Verification of the flow and sensitivity solvers, the adaptive procedure, the error estimators and any post-processing procedure. To our knowledge, this is the first reported Verification by the MMS of sensitivity solver for wall-bounded turbulent flows. This first step is mandatory to establish the correctness and reliability of the numerical techniques developed especially given the complexity of the problem at hand. Furthermore, comparisons with experiments as the ones presented in Section 8 would be totally irrelevant without performing first Code and Solution Verification as reported in the literature [27,45].

7.1. Definition of the Manufactured Solution

The Manufactured Solution (MS) mimics the near-wall behavior of a two-dimensional, steady incompressible turbulent boundary-layer. The Reynolds number Re defined by $Re = \frac{U_1 L}{\nu}$, where U_1 is the reference velocity, L the reference length and ν the kinematic viscosity, is set to one million. This Manufactured Solution has been used for the 2nd Workshop on CFD Uncertainty Analysis [45] to perform Code Verification and to assess the accuracy of some error estimators. The Manufactured Solution and the source terms defining the modified problem are thoroughly described in Refs. [46,47]. These manufactured source terms are incorporated in $\mathbf{f}$, $q_{\mathcal{K}}$ and $q_{\mathcal{E}}$ in Eqs. (1), (5) and (6) respectively. The mass conservation equation (2) is left

unchanged since the manufactured velocity field is solenoidal. Additional source terms are required for Verification of wall functions as detailed in Ref. [48].

In the present study, we extend the Manufactured Solution to perform Verification of shape sensitivity problems with wall functions. We focus on sensitivity of the flow response with respect to the vertical position of the flat wall along which the turbulent boundary-layer develops. The problem is illustrated in Fig. 2 where y_0 is the shape parameter of interest. The manufactured sensitivity fields are obtained by explicit differentiation of the manufactured flow solution with respect to y_0. From these sensitivity fields, the source terms for the modified sensitivity problem are derived according to the Method of the Manufactured Solution and incorporated in $\mathbf{f}^s, q_K^s$ and q_ε^s in Eqs. (18), (20) and (21) respectively.

For completeness, we briefly describe the manufactured flow and sensitivity fields. As illustrated in Fig. 2, the physical domain is a square of side $0.5L$ with $0.5L \leqslant x \leqslant L$ and $0 \leqslant y - y_0 \leqslant 0.5L$. All quantities presented below are non-dimensional using L and U_1 as the reference length and velocity scale. In the definition of the velocity components and pressure coefficient, we use the following *similarity variables* with $\sigma = 4.$ and $\sigma_v = 2.5\sigma$:

$$\eta = \frac{\sigma(y - y_0)}{x} \quad ; \quad \eta_v = \frac{\sigma_v(y - y_0)}{x} \tag{34}$$

The streamwise velocity component, u and the normal velocity component, v, are given by:

$$u = \mathrm{erf}(\eta) \tag{35}$$

$$v = \frac{1}{\sigma\sqrt{\pi}}(1 - e^{-\eta^2}) \tag{36}$$

and the pressure is taken to be:

$$p = 0.5\ln(2x - x^2 + 0.25)\ln(4y^3 - 3y^2 + 1.25) \tag{37}$$

The manufactured field of k and ϵ are generated using the following equations:

$$k = k_{max}\eta_v^2 e^{1-\eta_v^2} + \alpha_k \tag{38}$$

$$\epsilon = 0.36\frac{k_{max}^2}{v_{max}} e^{-\eta_v^2} + \alpha_\epsilon \tag{39}$$

with $k_{max} = 0.01$ and $v_{max} = 0.001$. Finally, the eddy-viscosity is obtained from Eq. (3). Note that in Eqs. (38) and (39), we have added small constants α_k and α_ϵ to the manufactured fields for k and ϵ compared to what is described in Ref. [46]. This has been done to avoid logarithms of zero values since the computational variables for the turbulence model are the logarithms of k and ϵ. These constants have been chosen so as to have a negligible effect on the Manufactured Solution as explained in Ref. [44].

$$\alpha_k = 10^{-5}; \quad \alpha_\epsilon = 10^{-3} \tag{40}$$

The analytical solution for all variables is imposed on the inflow and upper boundaries as Dirichlet boundary conditions. On the outlet, the normal and tangential forces on the boundary are imposed from the exact velocity and pressure fields. The diffusion fluxes of k and ϵ are also imposed from the exact solution. Hence, on the outlet Neumann boundary conditions are applied on all variables. On the computational wall (bottom) boundary, the type of boundary conditions is determined by the wall functions (see Section 3.2):

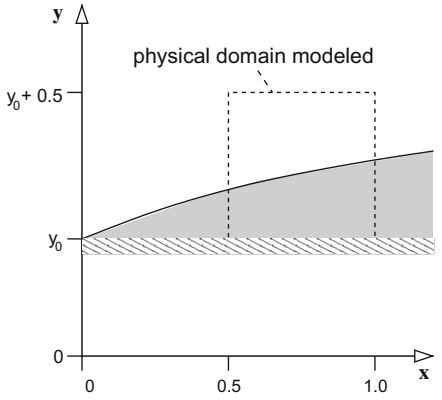

Fig. 2. Manufactured problem: computational domain.

- u: Robin boundary condition
- v: Dirichlet boundary condition
- k: Neumann boundary condition
- ϵ: Dirichlet boundary condition

As described in Ref. [48], source terms are added in the classical wall function boundary conditions for compatibility with the Manufactured Solution. The computational boundary is set at a distance $d = 0.006$ from the true wall located at $y = y_0$. This ensures, for a Reynolds number of one million, that the non-dimensional wall distance in viscous unit, y^+, (see Eq. (11)) lies in [30,300] on all the wall while being as close as possible of the lower limit.

Direct differentiation of the Manufactured Solution with respect to y_0 yields the following expressions for the sensitivities of the flow and turbulent variables:

$$S_u = -\frac{2\sigma}{x\sqrt{\pi}} e^{-\eta^2}$$

$$S_v = -\frac{2\eta}{x\sqrt{\pi}} e^{-\eta^2}$$

$$S_p = \frac{3(y-yo)[1-2(y-yo)]}{4(y-yo)^3 - 3(y-yo)^2 + 1.25} \log(2x - x^2 + 0.25)$$

$$S_k = \frac{2k_{max}\sigma_v}{x} \eta_v(\eta_v^2 - 1) e^{(1-\eta_v^2)}$$

$$S_\epsilon = \frac{0.72k_{max}^2\sigma_v}{xv_{max}} \eta_v e^{-\eta_v^2}$$

The boundary conditions for the sensitivity problem are deduced from the flow boundary conditions described above (see Section 5.3 for more details).

7.2. Verification of flow and sensitivity solutions

The flow and sensitivity fields are solved using the adaptive finite-element method presented in Section 6. All flow and sensitivity variables contribute to the error estimation so that the mesh adaptation process is driven by 10 error estimators (velocity, pressure, k, ϵ and μ_t and their corresponding sensitivities). Eight grid adaptation cycles have been performed. Fig. 3 shows the final mesh containing 123,689 nodes. It is typical of adapted meshes for boundary-layer flow problems. As expected, extensive refinement is observed in the near-wall region. Several bands of refinement can also be identified which correspond to regions of rapid variation in velocity, $\mathcal{K}, \mathcal{E}$ and μ_t and their sensitivities.

Fig. 4 presents the trajectories of semi-norms of the true and estimated error for the flow variables and their sensitivities. The semi-norms are defined as follows:

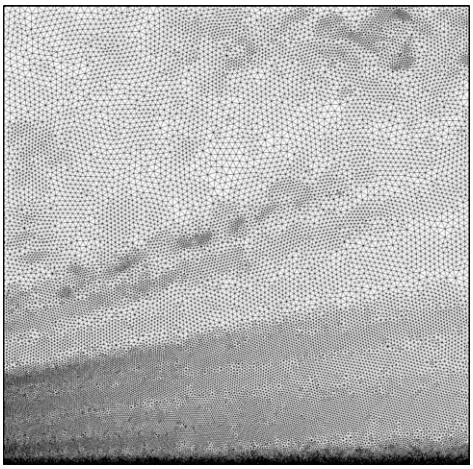

Fig. 3. Manufactured Solution: final adapted mesh.

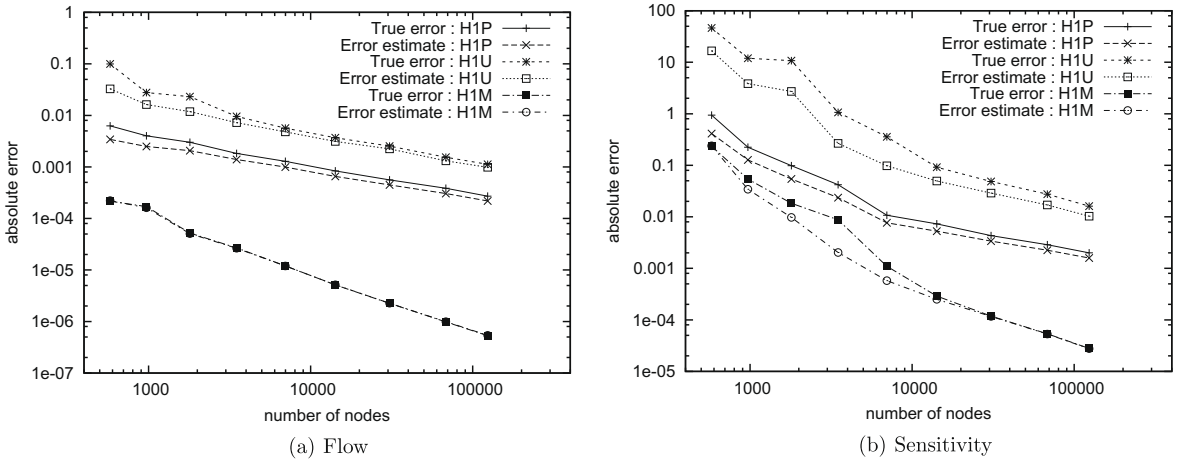

Fig. 4. Manufactured Solution: trajectories of true and estimated error norms.

$$\text{H1U} : \|\mathbf{e_u}\| = \sqrt{\int_\Omega (\nabla e_u \cdot \nabla e_u + \nabla e_v \cdot \nabla e_v)\, d\Omega}$$

$$\text{H1P} : \|e_p\| = \sqrt{\int_\Omega \nabla e_p \cdot \nabla e_p \, d\Omega}$$

$$\text{H1M} : \|e_{\mu_t}\| = \sqrt{\int_\Omega \nabla e_{\mu_t} \cdot \nabla e_{\mu_t} \, d\Omega}$$

with $\mathbf{e_u} = [e_u, e_v]^T = [u - u_h, v - v_h]^T$, $e_p = p - p_h$ and $e_{\mu_t} = \mu_t - \mu_{th}$ where the subscript h referred to discrete finite-element solutions. The true error is computed using the exact manufactured fields and the estimated error is obtained from the ZZ error estimator as described in Section 6.

As can be seen in Fig. 4, errors on both the flow and the sensitivity decrease from cycle to cycle indicating the correct implementation of both the numerical discretization and the adaptive strategy. Moreover, the trajectory of the error estimates almost converges to that of the true errors with mesh adaption. Indeed, the efficiency indexes of the ZZ error estimators are close to one (actually between 0.85 and 1.05) as reported in [44]. This property implies that the error estimators become more accurate and reliable with mesh refinement which in turns allows for appropriate mesh adaptation. Furthermore, it is worth noting that the observed orders of convergence for all dependent variables are in the range of what was theoretically expected (see [44] for details).

We now turn our attention to the evaluation the friction resistance R_f on the wall boundary (Γ_w) and its sensitivity since such quantities are the most demanding to predict accurately. Furthermore, it will allow for the verification of the post-processing procedure at hand. Taking $\rho U_{\text{ref}}^2 L_{\text{ref}}$ as a reference force, the friction resistance is computed as follows:

$$R_f = \frac{1}{\rho U_{\text{ref}}^2 L_{\text{ref}}} \int_{\Gamma_w} \tau \cdot \hat{\mathbf{n}} \cdot \hat{\mathbf{t}} \, d\Gamma = \int_{\Gamma_w} \left[(\mu + \mu_t) \left(\frac{\partial u}{\partial y} + \frac{\partial v}{\partial x} \right) \right] d\Gamma$$

The last integral is a simplified expression for our particular case using $\hat{\mathbf{n}} = [0,1]^T$; $\hat{\mathbf{t}} = [1,0]^T$.

Explicit differentiation of the above expression yields the sensitivity of the friction coefficient which is an Eulerian (partial) derivative with respect to the parameter y_0. For this problem, the geometric sensitivities are:

$$\frac{\partial \hat{\mathbf{n}}}{\partial y_0} = \frac{\partial \hat{\mathbf{t}}}{\partial y_0} = [0,0]^T; \quad \frac{\partial \widehat{\mathbf{X}}}{\partial y_0} = [0,1]^T \tag{41}$$

which leads to the following simplified expression for the Eulerian sensitivity of the friction resistance:

$$\frac{\partial R_f}{\partial y_0} = \int_{\Gamma_w} \left[(\mu + \mu_t) \left(\frac{\partial S_u}{\partial y} + \frac{\partial S_v}{\partial x} \right) + \mu_t' \left(\frac{\partial u}{\partial y} + \frac{\partial v}{\partial x} \right) \right] d\Gamma \tag{42}$$

The Lagrangian (total) sensitivity is easily derived using the total derivative with respect to the parameter y_0. In our particular case, the expression can be simplified to:

$$\begin{aligned} \frac{DR_f}{Dy_0} &= \frac{1}{\rho U_{\text{ref}}^2 L_{\text{ ref}}} \int_{\Gamma_w} \frac{D\tau}{Dy_0} \cdot \hat{\mathbf{n}} \cdot \hat{\mathbf{t}} \, d\Gamma = \frac{1}{\rho U_{\text{ref}}^2 L_{\text{ ref}}} \int_{\Gamma_w} \left(\frac{\partial \tau}{\partial y_0} + \nabla \tau \cdot \frac{\partial \widehat{X}}{\partial y_0} \right) \cdot \hat{\mathbf{n}} \cdot \hat{\mathbf{t}} \, d\Gamma \\ &= \frac{\partial R_f}{\partial y_0} + \frac{1}{\rho U_{\text{ref}}^2 L_{\text{ref}}} \int_{\Gamma_w} \nabla \tau \cdot \frac{\partial \widehat{X}}{\partial y_0} \cdot \hat{\mathbf{n}} \cdot \hat{\mathbf{t}} \, d\Gamma = \frac{\partial R_f}{\partial y_0} + \frac{1}{\rho U_{\text{ref}}^2 L_{\text{ref}}} \int_{\Gamma_w} \left[(\mu + \mu_t) \left(\frac{\partial^2 u}{\partial y^2} + \frac{\partial^2 v}{\partial xy} \right) + \mu_t' \left(\frac{\partial u}{\partial y} + \frac{\partial v}{\partial x} \right) \right] d\Gamma \end{aligned} \tag{43}$$

As can be seen, the Lagrangian sensitivity $\frac{DR_f}{Dy_0}$ is equal to the Eulerian sensitivity $\frac{\partial R_f}{\partial y_0}$ plus a transpiration term (last integral term of the third and fourth lines) which accounts for the change in the position of the wall boundary caused by changes in the parameter y_0. Since the wall boundary condition does not depend on y_0, its Lagrangian derivative is zero. This is confirmed by Table 2 which gives the exact analytical value of the friction coefficient and its sensitivities. This means that the transpiration term (last term of the fourth line in Eq. (43)) exactly cancels out the Eulerian sensitivity given by Eq. (42). This can easily be seen since $\frac{\partial \cdot}{\partial y} = -\frac{\partial \cdot}{\partial y_0}$.

Fig. 5 shows the evolution of the true errors in R_f and its sensitivities with adaptive cycles. As can be seen, the errors decrease from cycle to cycle. Hence, the errors on the sensitivity of boundary integral forces can be reduced as much as desired using the adaptive process. Indeed, the prediction of the friction coefficient on the first coarse mesh is marred with a relative true error greater than 150% and 600% for its Eulerian sensitivity. These relative errors are reduced to less than 0.004% and 0.03% on the last adapted mesh.

We take advantage of the MS to illustrate how sensitivity information can be used for the evaluation of solution on nearby geometries and to assess the accuracy of this procedure. We use first order Taylor-series expansions of the flow response in parameter space to approximate the flow for which the flat plate is located at $y_0 + \delta y_0$ using only information at the baseline state (for which the flat plate is located at y_0):

$$\phi(\mathbf{x}; y_0 + \delta y_0) \approx \phi(\mathbf{x}; y_0) + \delta y_0 \frac{\partial \phi}{\partial y_0}(\mathbf{x}; y_0)$$

We consider a change of $\delta y_0 = 0.02$ in the shape parameter from its baseline value of zero and we compare the baseline flow, the first order extrapolation from $y_0 = 0$ to $y_0 + \delta y_0 = 0.02$ and the recomputed flow at $y_0 = 0.02$ (reanalysis with the flow solver). Fig. 6 shows the transverse distributions of the horizontal velocity component u, the normal velocity component v and the pressure p at the outlet ($x = 1$). The baseline and extrapolated solutions are available on the baseline domain i.e. $y \in [0.006, 0.5]$ while the recomputed solution is available on the perturbed domain i.e. $y \in [0.026, 0.52]$ corresponding to the shaded area in Fig. 6. Note that the extrapolated solution for $y \in [0.006, 0.026]$ has no direct physical meaning.

As can be seen, the agreement between reanalysis and extrapolation results is almost perfect. This first shows that the numerical evaluation of the flow sensitivities is accurate. Second, it tells us that the change in the shape parameter is sufficiently small to ensure that the linear Taylor-series in parameter space is a reliable approximation of the flow variable dependence on y_0, in spite of the apparently complicated relationships given by Eqs. (35)–(39).

8. Application to turbulent flow around a square obstacle

8.1. Definition of the problem

We consider the flow of air around a cylinder of square cross-section in the proximity of a solid wall as investigated by Wu and Martinuzzi using Laser Doppler Velocimetry [49]. The experimental configuration consists of a smooth flat plate

Table 2
Manufactured Solution: friction resistance.

Exact friction coeff.	Exact Eulerian sensitivity	Exact Lagrangian sensitivity
$R_f = 0.354686 \times 10^{-5}$	$\frac{\partial R_f}{\partial y_0} = -0.267451 \times 10^{-3}$	$\frac{DR_f}{Dy_0} = 0$

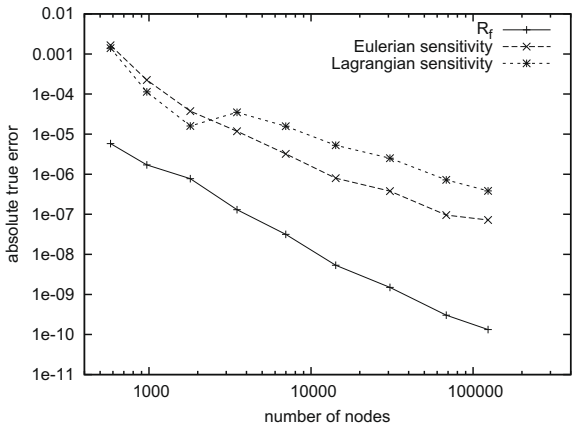

Fig. 5. Trajectories of the true errors in R_f and its sensitivities.

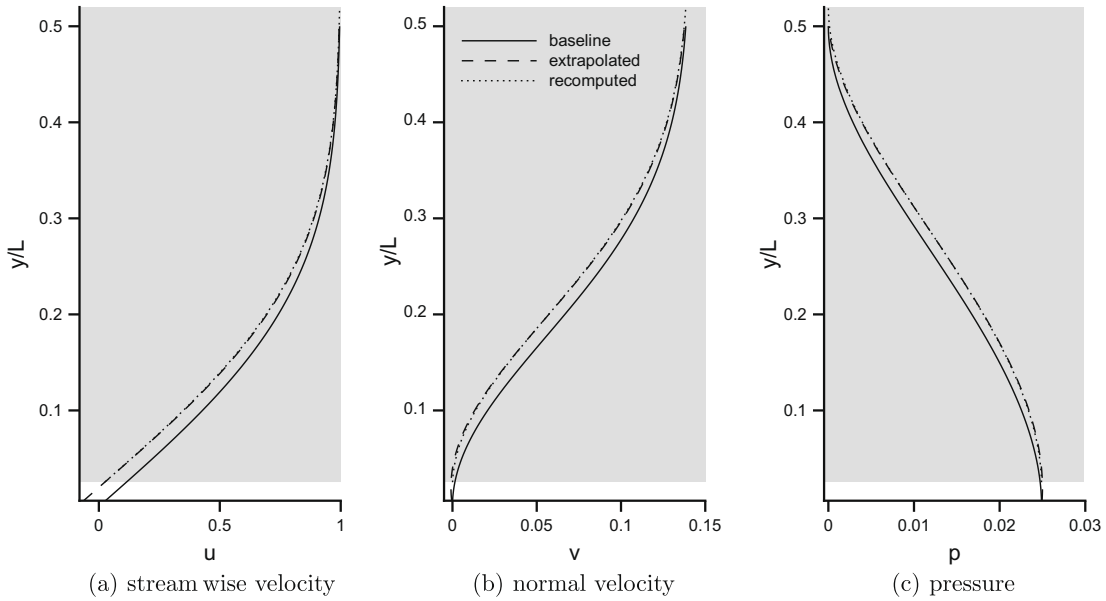

Fig. 6. Baseline, extrapolated and recomputed isolines.

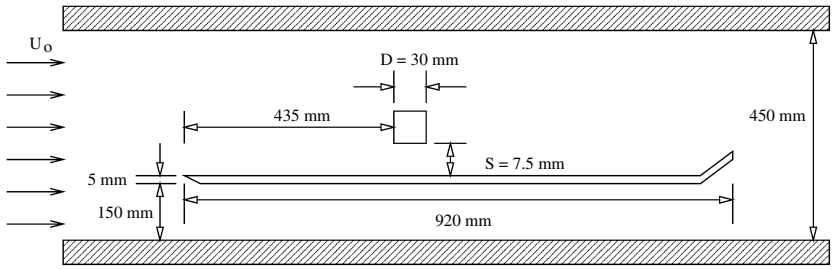

Fig. 7. Experimental set-up.

located in the 0.45 m × 0.45 m test section of a suction-type wind tunnel. Details of the experimental set-up are shown in Fig. 7. Experiments were conducted for a Reynolds number of 22,000 based on D, the dimension of the side of the square obstacle, and U_0, the inlet velocity. The oncoming free stream turbulence intensity is set at 1% and the mean flow is steady.

In the remainder of the article, all quantities presented are non-dimensionalized with D and U_0 as the reference length and velocity scale.

8.2. Computational domain and Sensitivity Analysis

The computational domain and boundary conditions are shown in Fig. 8. In the experiment, an end-plate flap was adjusted to maintain parallel flow below the plate. However, it is generally assumed that the flow above the plate is not influenced by the flow under the plate. Hence, only the portion of the tunnel located above the plate is included in the computational model. Also it was deemed unnecessary to simulate the effect of the end-plate flap.

Wall functions provide boundary conditions along the solid surfaces of the domain: upper wall of the tunnel, the sides of the obstacle, and the plate. As was shown in a previous study [50], it is necessary to include the thickness of the real plate in the computational model in order to reproduce the physically observed stagnation point at the leading edge of the plate. The half-thickness of the plate model is therefore set to 0.083. With this model geometry, the production of k, which depends on the velocity gradients, is triggered a short distance upstream of the leading edge of the plate so that realistic levels of turbulence are reproduced in this region. The leading edge of the plate, as well as the corners of the cylinder, are rounded to avoid corner singularities with wall functions.

The inlet value of k is set to achieve an inflow with a turbulence intensity of 1%. Based on previous experience [50], the inlet value of ϵ is adjusted so that the inlet eddy-viscosity is equal to ten times the molecular viscosity.

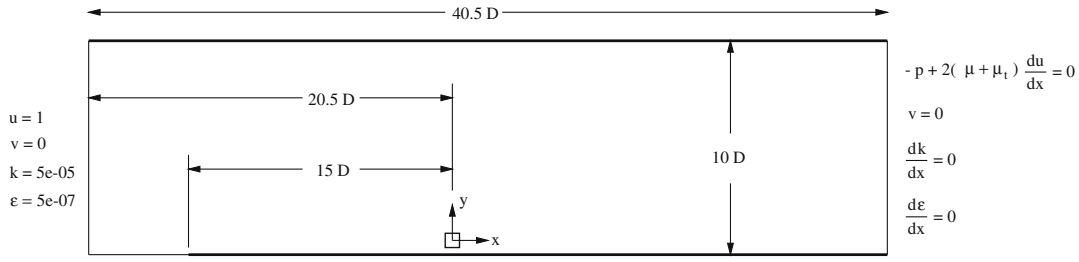

Fig. 8. Computational domain and boundary conditions.

First, in Section 8.3, we proceed with Verification and Validation of our simulation results. In Section 8.4, verified sensitivity predictions are used to assess the effect of reducing the gap S between the obstacle and the flat plate. The baseline value of $S = S_0 = 0.25$ combines with perturbations that reduce the value of S guarantee that all configurations will remain in the steady state flow regime observed experimentally [49]. Perturbations in the parameter S only affect the geometry of the obstacle. Hence, geometric sensitivities are zero on all boundaries except that of the obstacle where:

$$\frac{\partial \hat{\mathbf{n}}}{\partial S} = \frac{\partial \hat{\mathbf{t}}}{\partial S} = [0,0]^T; \quad \frac{\partial \hat{\mathbf{X}}}{\partial S} = [0,-1]^T \tag{44}$$

8.3. Numerical results: Solution Verification and Validation

Mesh independent flow and sensitivity solutions are obtained by the adaptive remeshing procedure. Solutions are considered mesh independent when no major changes occur with further mesh refinement. The final mesh, after 8 adaptive remeshings, has 556, 567 nodes. Figs. 9 and 10 show the 6th mesh generated by the adaptive process with approximately 220,000 nodes (the 8th mesh being too fine to be of any visual interest once displayed in a figure). Recall that the mesh is adapted to both the flow and sensitivity variables. However, several regions of high refinement can be easily related with

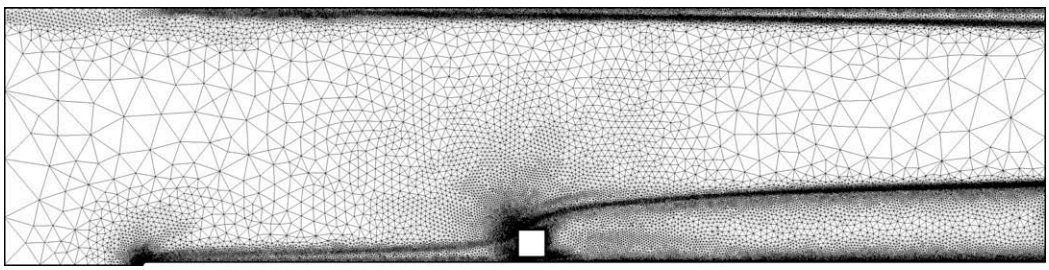

Fig. 9. Mesh after 6 cycles of adaption.

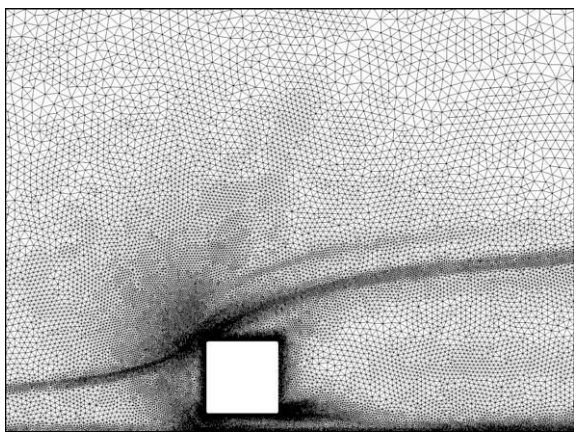

Fig. 10. Mesh after 6 cycles of adaption near obstacle.

some flow features: the rapid variation of the solution close to the leading edge of the plate, the upper and lower edges of the boundary-layers developing on the flat plate and upper wall, the shear layer emanating from the corners of the obstacle, etc.

We now turn our attention to assess whether a grid converged solution has been achieved (Solution Verification). Fig. 11(a) shows the convergence of the distribution of the non-dimensional distance to the wall, as defined by Eq. (11), along the flat plate with adaptive cycles. As can be seen, mesh independent boundary conditions are achieved and all values of y^+ satisfy the condition $30 < y^+ < 300$. This is indeed important to ensure a proper modeling of the flow with wall functions. Although not illustrated here, similar observations hold for the distributions of y^+ along all wall boundaries. Fig. 11(b) shows the convergence of the drag and lift coefficients with the number of nodes. As can be seen, grid converged coefficients are quickly reached.

Fig. 12(a) and (b) shows the distribution of the skin friction along the plate and that of its sensitivity with adaptive cycles. Once again, grid converged distributions are achieved by the adaptive procedure. As can be seen, the grid converged distribution of c_f presents a first peak near the leading edge of the plate ($x = -15$) and a second one in the vicinity of the obstacle due to the fluid being squeezed in the channel under the obstacle. The magnitude of the sensitivity seen in Fig. 12(b) indicates that any change in the value of S will have a significant effect on the skin friction near the obstacle. The nearly zero value upstream of the square indicates the changes in S have no impact on c_f in this region. However, this plot shows that a reduction of the gap size results in sharp increases of the skin friction near the obstacle. The negative values of sensitivity downstream the obstacle indicates a reduction of the skin friction in this area. These results indicate that the adaptive procedure has produced verified flow predictions in the sense of Roache [27].

We now compare numerical flow predictions to available experimental data of Wu and Martinuzzi (Validation). In what follows, all predicted solutions have been verified as grid converged. For clarity and brevity we do not include plots showing grid independence for all flow quantities. Since Code and Solution Verification have been performed first, we can state that the observed discrepancies between the numerical solution and the experimental data are due to the limitations of the turbulence modeling (modeling error). Transverse profiles downstream of the cylinder at $x = 1$ of the mean velocity components, u and v, and of the streamwise and shear components of the Reynolds stress, $-\overline{u'u'}$ and $-\overline{u'v'}$ are presented in Figs.

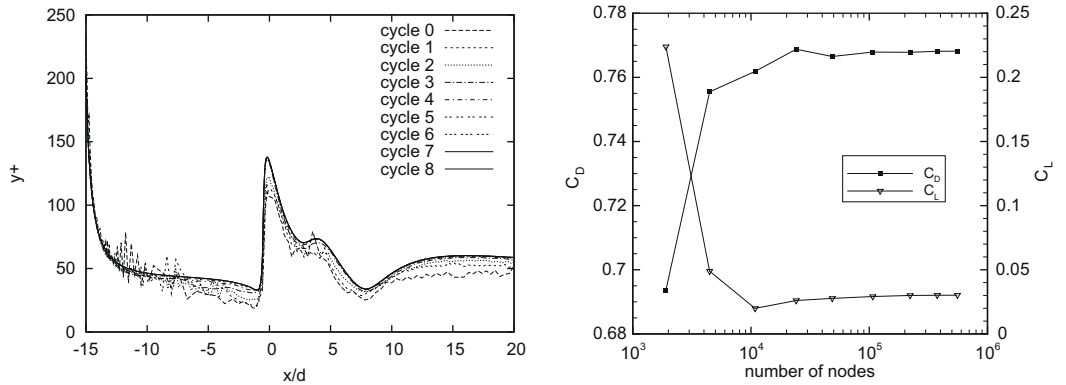

(a) Distribution of y^+ along the plate (b) Loads on the square cylinder

Fig. 11. Grid convergence with adaptive cycles.

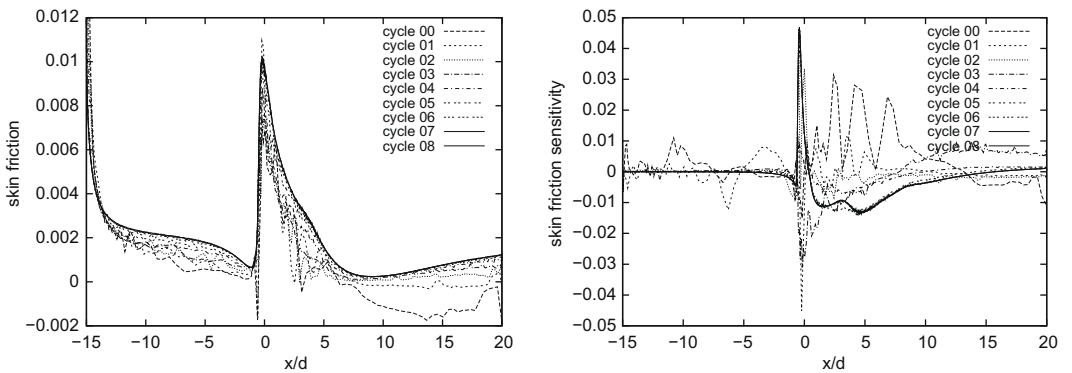

(a) Skin friction c_f (b) Sensitivity of c_f

Fig. 12. Skin friction and its sensitivity along the plate with adaptive cycles.

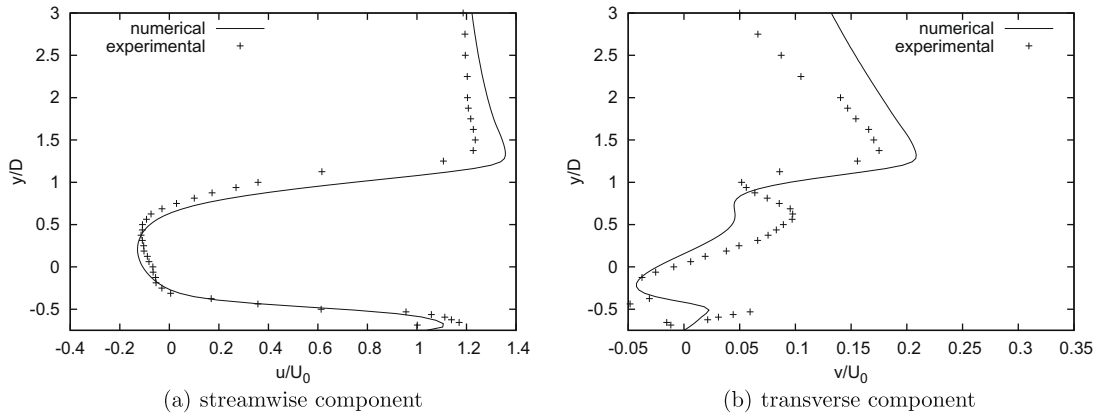

(a) streamwise component (b) transverse component

Fig. 13. Comparison of velocity profiles with experiments at $x = 1$.

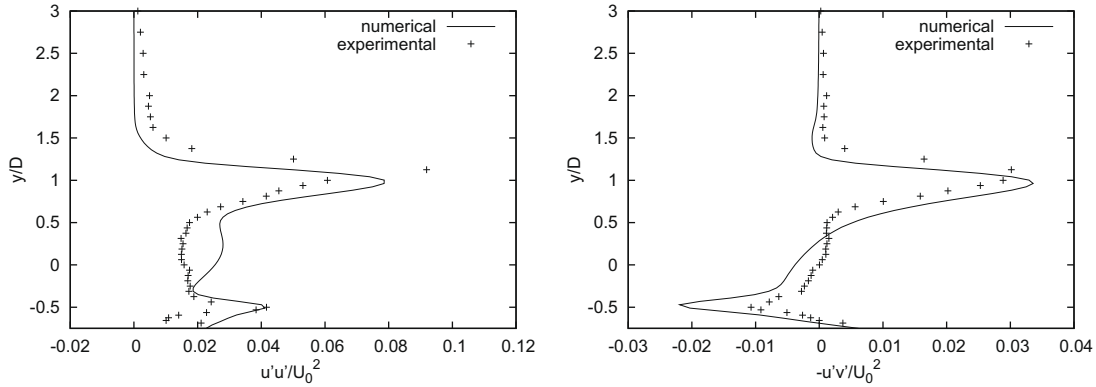

(a) streamwise normal component (b) shear component

Fig. 14. Comparison of Reynolds stress profiles with experiments at $x = 1$.

13 and 14. The best prediction are obtained for u though the strength of the wall jet caused by the flow in the gap under the cylinder is slightly under-predicted. For the other quantities, the numerical results capture the major trends observed in the measurements but with some significant discrepancies in magnitude indicating that the turbulence model cannot reproduce completely the flow physics.

8.4. Numerical results: Sensitivity Analysis

Fig. 15 presents streamlines for the flow velocity (computed from $\mathbf{u} = [u, v]^T$) and for its sensitivity (obtained from the velocity sensitivity $\mathbf{s_u} = [s_u, s_v]^T$). The flow streamlines in Fig. 15(a) clearly show the fluid flowing upwards on the vertical face of the obstacle, turning smoothly around the corner and being entrained at a positive angle by the main flow. In Fig. 15(b), the transpiration terms in the boundary conditions for the sensitivity problem with respect to shape parameters is clearly visible. For example, some sensitivity streamlines intersect the boundary. Recall that the Sensitivity Equations were solved for a reduction of the gap size, that is when the obstacle is being lowered, and that we consider Eulerian sensitivity. According to the flow sensitivity streamlines in Fig. 15(b), lowering the block will have the following consequences on the flow:

(1) The fluid that is just ahead of the obstacle will flow more easily with the main flow when the obstacle is lowered. Velocity streamlines will point diagonally upwards from left to right as it is predicted by the streamlines of the sensitivity of the velocity.
(2) The sensitivity streamlines pointing downwards to and intersecting the rounded edge indicate the following: the space is freed by lowering the block so that the upper part of the flow on the front face will turn right to head downstream at a lower height than that of the baseline configuration. Thus the fluid flowing around the top corner no longer has to take such a long detour and the velocity vector will be at a shallower angle with respect to the horizontal. Sensitivity streamlines reflect this by pointing downwards.

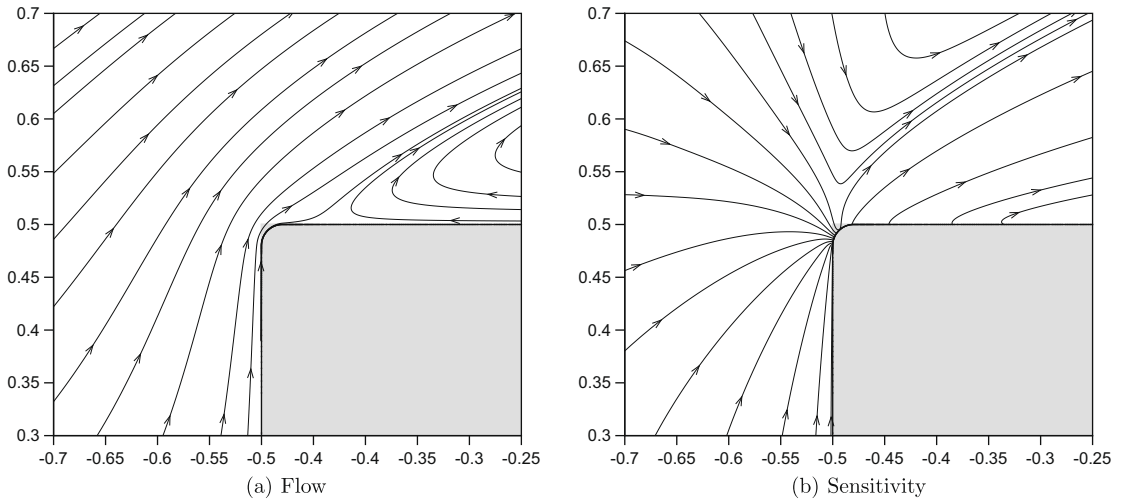

Fig. 15. Streamlines of the flow velocity and its sensitivity near top left corner.

(3) Lowering the obstacle will allow fluid that was attached to the top of the obstacle to be entrained by the main flow. Sensitivity streamlines emanating from the boundary simply tell us that the flow velocity streamlines will be pointing diagonally upwards since space will be freed to make room for the flow.

Note also that the velocity sensitivity vector is tangent to the vertical walls of the square cylinder (see Fig. 15(b)). This was expected from theoretical considerations. The idea behind that is similar to the finding of Ilinca and Pelletier [3] who first demonstrated that when a homogeneous Dirichlet boundary condition applies on a boundary for the flow velocity ($\mathbf{u} = \mathbf{0}$, i.e. no slip wall), the normal component of the velocity sensitivity is zero at the boundary ($\mathbf{s_u} \cdot \hat{\mathbf{n}} = 0$). Here, we use wall functions to model the flow in the viscous sub-layers of solid walls so that this result does not apply. However, by choosing the unit vector triad $(\hat{\mathbf{t}}, \hat{\mathbf{n}}, \mathbf{e_z})$ positively oriented (right-handed) and using the flow incompressibility condition Eq. (2), the flow sensitivity boundary condition in the normal direction Eq. (31) at computational walls can be rewritten as:

$$\mathbf{s_u} \cdot \hat{\mathbf{n}} = -\left[(\nabla \mathbf{u} \cdot \hat{\mathbf{t}}) \times \frac{\partial \widehat{\mathbf{X}}}{\partial a}\right] \cdot \mathbf{e_z} - \mathbf{u} \cdot \frac{\partial \hat{\mathbf{n}}}{\partial a} \tag{45}$$

where $\times$ is the right-handed vector cross product. Here, given the sensitivities of geometric quantities for the shape parameter at hand (see Eq. (44)), the right-hand side reduces to the derivative of the streamwise component of the velocity in the tangential direction which is zero on vertical walls according to the flow boundary condition in the normal direction at computational walls.

8.5. Numerical results: Uncertainty Analysis

We now perform Uncertainty Analysis on input data using sensitivity information. We derive error bars on the friction coefficient along the flat plate due to uncertainties on the gap size value from:

$$\delta c_f = \pm \frac{\partial c_f}{\partial S} |\delta S|$$

Fig. 16 shows the friction coefficient distribution with error bars corresponding to 1%, 3%, 5% and 7% of relative uncertainties on the gap size. As can be seen, the uncertainty on c_f is negligible for 1% in comparison to experimental uncertainties. However, it becomes noticeable for gap size uncertainties larger than 3%. For 7%, the uncertainty on the friction coefficient reaches values up to 10% of the nominal prediction in the area around the square cylinder.

Finally, we use a first-order Taylor-series expansion in S to provide fast and inexpensive estimates (as compared to full-blown flow reanalysis) of the velocity and Reynolds stress profiles in the case of a 10% reduction in the gap size. The extrapolated profiles are compared to those obtained by a full simulation (reanalysis) at the perturbed value of the gap size. For example, we compare the extrapolated profile obtained from the first-order expansion of the streamwise velocity component u:

$$u(y; S_0 + \delta S) \approx u(y; S_0) + \delta S \frac{\partial u}{\partial S}(y; S_0) \tag{46}$$

with the *true* profile extracted from a simulation at $S = S_0 + \delta S$. Figs. 17 and 18 show the results of this extrapolation for streamwise and transverse velocity components u and v as well as for the Reynolds stress components $-\overline{u'u'}, -\overline{u'v'}$ and

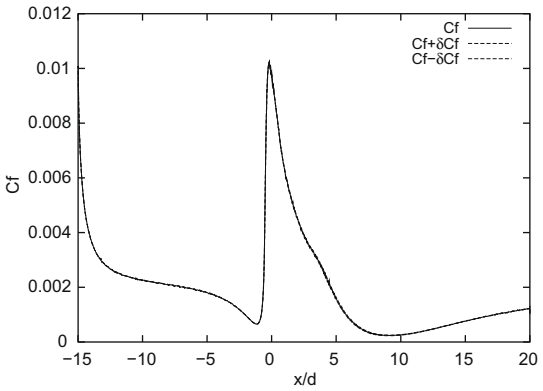

(a) 1%

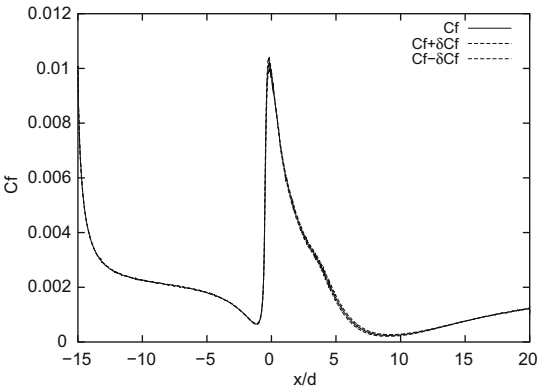

(b) 3%

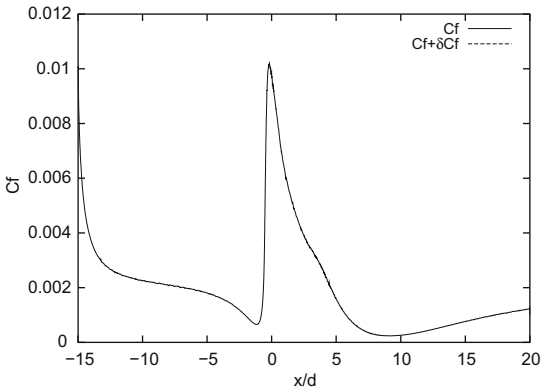

$-\overline{v'v'}$ for $\delta S = -10\% S_0$ at $x = 4$. The dotted line is the baseline solution obtained at $S = S_0$, the solid line is the recomputed solution at the perturbed state $S = S_0 + \delta S$ and the dashed line is the fast prediction using Taylor-series expansion in the parameter space. As can be seen, the agreement of the extrapolated estimates with the recomputed solution is remarkably good for a perturbation as large as 10% of the shape parameter baseline value which results in significant changes in the flow response.

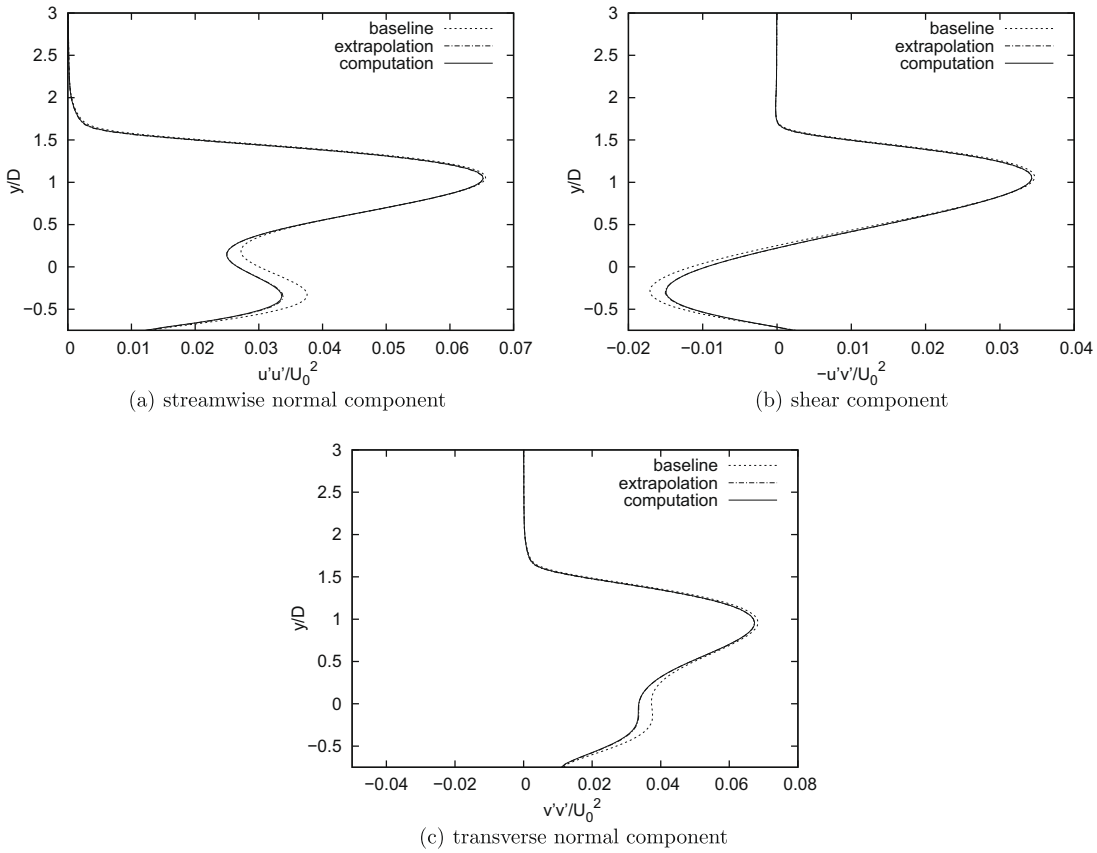

Fig. 18. Ten percent Reynolds stress extrapolation at $x = 4$.

Note that more complex parameter dependency of the flow response or extrapolation further in the parameter space may require second-order sensitivity (see Ref. [51]).

9. Conclusions

A general Sensitivity Equation Method was presented for the k–ϵ model of turbulence with wall functions. It covers both value and shape parameters. For the latter, a proper description of geometric quantities is required since boundaries are parameter dependent. However, the main challenge encountered is the proper derivation and evaluation of the boundary conditions for the Eulerian sensitivity. In particular, the differentiation of the wall functions for the flow to obtain wall functions for the Sensitivity Equations is a tedious task. Furthermore, it reveals that one must evaluate first and second derivatives of the solution fields at the computational boundary. This was done through a constrained Taylor-series least-squares procedure to yield accurate spatial flow derivatives in the sensitivity boundary conditions.

An adaptive finite-element method driven by a posteriori estimates of the error on all variables was used to produce accurate and grid independent flow and sensitivity solutions.

Code Verification was performed using a Manufactured Solution, including wall functions, mimicking a turbulent boundary-layer on a flat plate presented in [46] and extended here to address the shape parameter sensitivity problem. Results from a grid adaptive refinement study indicate that flow and sensitivity solvers, error estimators and the adaptive strategy are verified in the sense of Roache [27].

The methodology was applied to turbulent flows past a square obstacle in ground proximity and partly immersed in the boundary-layer. Solution Verification and Validation were first performed to establish the accuracy of the numerical predictions. Then, sensitivity study of the effect of gap size on the flow was carried out. The grid converged solutions of the CSE reproduces the expected and computed trends of the flow response when the gap size is reduced. Sensitivity informations were used to estimate uncertainties of the flow response caused by uncertainties in the shape parameter. Finally, it was shown that sensitivity-based first order extrapolation in the parameter space yields accurate (and inexpensive) estimates of flows on nearby geometries.

Acknowledgments

This work was supported in part by the Canadian Research Chair Program and by the National Science and Engineering Council of Canada (NSERC, Government of Canada).

References

[1] E.J. Nielsen, W.K. Anderson, Aerodynamic design optimization on unstructured meshes using the Navier–Stokes equations, AIAA J. 37 (11) (1999) 1411–1419.
[2] M. Nemec, D.W. Zingg, T.H. Pulliam, Multi-point and multi-objective aerodynamic shape optimization, AIAA J. 42 (6) (2004) 1057–1065.
[3] F. Ilinca, D. Pelletier, A continuous shape sensitivity equation method for unsteady laminar flows, Int. J. Comput. Fluid Dyn. 21 (7–8) (2007) 255–266.
[4] S.-Y. Lu, P. Sagaut, Direct sensitivity analysis for smooth unsteady compressible flows using complex differentiation, Int. J. Numer. Meth. Fluids 53 (12) (2007) 1863–1886.
[5] W.K. Anderson, J.C. Newman, D.L. Whitfield, E.J. Nielsen, Sensitivity analysis of Navier–Stokes equations on unstructured meshes using complex variables, AIAA J. 39 (1) (2001) 56–63.
[6] J. Borggaard, J. Burns, Asymptotically consistent gradients in optimal design, in: MDO – State of the Art; Proceedings of the ICASE/NASA Langley Workshop, Hampton, Virginia, 1995.
[7] J. Borggaard, A. Verma, On efficient solutions to the continuous sensitivity equation using automatic differentiation, SIAM J. Sci. Comput. 22 (1) (2000) 39–62.
[8] A. Griewank, Some bounds on the complexity of gradients, Jacobians, Hessians, in: P. Pardalos (Ed.), Complexity in Nonlinear Optimization, World Scientific Publishers, River Edge, NJ, 1993.
[9] E. Laporte, P.L. Tallec, Numerical Methods in Sensitivity Analysis and Shape Optimization, Birkhäuser, Boston, 2003.
[10] B. Mohammadi, O. Pironneau, Shape optimization in fluid mechanics, Ann. Rev. Fluid Mech. 36 (2004) 255–297.
[11] D. Pelletier, Adaptive finite element computations of complex flows, Int. J. Numer. Meth. Fluids 31 (1999) 189–202.
[12] A. Hay, M. Visonneau, Adaptive finite-volume solution of complex turbulent flows, Comput. Fluids 36 (8) (2007) 1347–1363.
[13] J. Borggaard, J. Burns, A PDE sensitivity equation method for optimal aerodynamic design, J. Comput. Phys. 136 (2) (1997) 366–384.
[14] M.M. Tiller, J.A. Dantzig, Implementation of design sensitivity analysis and numerical optimization in engineering analysis, Appl. Math. Model. 20 (11) (1996) 792–799.
[15] J.C. Newman, A.C. Taylor, R.W. Barnwell, P.A. Newman, G.J.-W. Hou, Overview of sensitivity analysis and shape optimization for complex aerodynamic configurations, J. Aircr. 36 (1) (1999) 87–96.
[16] M.M. Putko, P.A. Newman, A.C. Taylor, L.L. Green, Approach for uncertainty propagation and robust design in CFD using sensitivity derivatives, in: 15th AIAA Computational Fluid Dynamics Conference, Anaheim, California, AIAA Paper 2001-2528, 2001.
[17] E. Turgeon, D. Pelletier, J. Borggaard, A general continuous sensitivity equation formulation for complex flows, Numer. Heat Transf. B 42 (6) (2002) 485–498.
[18] A. Hay, S. Etienne, R. Duvigneau, D. Pelletier, Evaluation of flows on nearby geometries by a shape sensitivity equation method, in: 44th AIAA Aerospace Sciences Meeting and Exhibit, Reno, Nevada, AIAA Paper 2006-1296, 2006.
[19] L.L. Green, P.A. Newman, K.J. Haigler, Sensitivity derivatives for advanced CFD algorithm and viscous modeling parameters via automatic differentiation, J. Comput. Phys. 125 (1996) 313–324.
[20] C.H. Bischof, H.M. Bücker, A. Rasch, Sensitivity analysis of turbulence models using automatic differentiation, SIAM J. Sci. Comput. 26 (2) (2004) 510–522.
[21] Z. Wang, D.A. Tortorelli, J.A. Dantzig, Sensitivity analysis and optimization of coupled thermal and flow problems with applications to contraction design, Int. J. Numer. Meth. Fluids 23 (1996) 991–1020.
[22] C.S. Kim, C. Kim, O.H. Rho, Sensitivity analysis for the Navier–Stokes equations with two-equation turbulence models, AIAA J. 39 (5) (2001) 838–845.
[23] A.G. Godfrey, E.M. Cliff, Sensitivity equations for turbulent flows, in: 39th AIAA Aerospace Sciences Meeting and Exhibit, Reno, Nevada, AIAA Paper 2001-1060, 2001.
[24] E. Turgeon, D. Pelletier, J. Borggaard, A general continuous sensitivity equation formulation for the k–epsilon model of turbulence, Int. J. Comput. Fluid Dyn. 18 (1) (2004) 29–46.
[25] E. Colin, S. Etienne, D. Pelletier, J. Borggaard, A general sensitivity equation formulation for turbulent heat transfer, Numer. Heat Transf. B 49 (2) (2006) 125–133.
[26] R. Duvigneau, D. Pelletier, On accurate boundary conditions for a shape sensitivity equation method, Int. J. Numer. Meth. Fluids 50 (2) (2006) 147–164.
[27] P.J. Roache, Verification and Validation in Computational Science and Engineering, Hermosa Publishers, Albuquerque, New Mexico, 1998.
[28] P.J. Roache, Code verification by the method of manufactured solutions, J. Fluids Eng. – Trans. ASME 114 (1) (2002) 4–10.
[29] P. Knupp, K. Salari, Verification of Computer Codes in Computational Science and Engineering, Chapman and Hall/CRC, 2003.
[30] F. Ilinca, D. Pelletier, Positivity preservation and adaptive solution for the $k-\epsilon$ model of turbulence, AIAA J. 36 (1) (1998) 44–51.
[31] B.E. Launder, J. Spalding, The numerical computation of turbulent flows, Comput. Meth. Appl. Mech. Eng. (1974) 269–289.
[32] J.-P. Chabard, Projet N3S – manuel de la version 3, tech. Rep. EDF HE-41/91.30B, Electricité de France, 1991.
[33] L. Ignat, D. Pelletier, F. Ilinca, Adaptive computation of turbulent forced convection, Numer. Heat Transf. A 34 (1998) 847–871.
[34] J.A. Schetz, Boundary Layer Analysis, Prentice Hall, 1993.
[35] M.C. Delfour, J.-P. Zolézio, Shapes and Geometries: Analysis, Differential Calculus and Optimization, Advances in Design and Control, vol. 4, SIAM, Philadelphia, 2001.
[36] M. Moubachir, J.-P. Zolézio, Moving Shape Analysis and Control: Applications to Fluid Structure Interactions, Chapman & Hall/CRC, Boca Raton, Florida, 2006.
[37] A.N. Brooks, T.J.R. Hughes, Streamline upwind/Petrov–Galerkin formulations for convection dominated flows with particular emphasis on the incompressible Navier–Stokes equations, Comput. Meth. Appl. Mech. Eng. 32 (1982) 199–259.
[38] F. Ilinca, J.-F. Hétu, D. Pelletier, On stabilized finite element formulations for incompressible advective–diffusive transport and fluid flow problems, Comput. Meth. Appl. Mech. Eng. 188 (1) (2000) 235–257.
[39] J. Peraire, M. Vahdati, K. Morgan, O. Ziekiewicz, Adaptive remeshing for compressible flow computations, J. Comput. Phys. 72 (2) (1987) 449–466.
[40] J.Z. Zhu, O.C. Zienkiewicz, A simple error estimator and adaptive procedure for practical engineering analysis, Int. J. Numer. Meth. Eng. 24 (1987) 337–357.
[41] J.Z. Zhu, O.C. Zienkiewicz, The superconvergent patch recovery and a posteriori error estimates, Int. J. Numer. Meth. Eng. 33 (1992) 1331–1364.
[42] M. Ainsworth, J.T. Oden, A Posteriori Error Estimation in Finite Element Analysis, Wiley & Sons, New York, 2000.
[43] R. Verfürth, A review of a posteriori error estimation and adaptive mesh refinement techniques, Wiley-Teubner, New York-Stuttgart, 1996.
[44] A. Hay, D. Pelletier, Code and solution verification of an adaptive finite element turbulent flow solver, in: 18th AIAA Computational Fluid Dynamics Conference, Miami, Florida, AIAA Paper 2007-4202, 2007.
[45] L. Eça, M. Hoekstra, P.J. Roache, Verification of calculations: an overview of the second Lisbon workshop, in: 18th AIAA Computational Fluid Dynamics Conference, Miami, Florida, AIAA Paper 2007-4089, 2007.

[46] L. Eça, M. Hoekstra, A. Hay, D. Pelletier, A manufactured solution for a two-dimensional steady wall-bounded incompressible turbulent flow, Int. J. Comput. Fluid Dyn. 21 (3–4) (2007) 175–188.
[47] L. Eça, M. Hoekstra, A. Hay, D. Pelletier, On the construction of manufactured solutions for one and two-equation eddy-viscosity models, Int. J. Numer. Meth. Fluids 54 (2) (2007) 119–154.
[48] L. Eça, M. Hoekstra, A. Hay, D. Pelletier, Verification of RANS solvers with manufactured solutions, Eng. Comput. 23 (2007) 253–270.
[49] K. Wu, R. Martinuzzi, Experimental study of the turbulent wake flow behind a square cylinder near a wall, in: ASME Fluids Engineering Division, Vancouver, British Columbia, 1997, No. FEDSM97-3151.
[50] D. Lacasse, É. Turgeon, D. Pelletier, On the judicious use of the $k-\epsilon$ model wall functions and adaptivity, Int. J. Thermal Sci. 43 (2004) 925–938.
[51] F. Ilinca, D. Pelletier, A. Hay, First- and second-order sensitivity equation methods for value and shape parameters, Int. J. Numer. Meth. Fluids 57 (2008) 1349–1370.